

Department of Anatomy and Histology
University of Veterinary Medicine, Budapest

**THREE-DIMENSIONAL MORPHOLOGICAL COMPARISON OF
FELINE TIBIAE**

By Cécile JESTIN

Supervisors:
Alexandre CARON, DVM, DipECVS
Balázs GERICS, PhD

Budapest, Hungary
2019

Table of Content

1. INTRODUCTION	1
1.1. Why choose Feline Tibia?	1
1.2. Objectives	1
1.3. Hypothesis	2
1.4. Reminder of Tibial Anatomy	2
2. MATERIALS AND METHODS	4
2.1. Bone collection and preparation	4
2.2. Computer Tomographic (CT) Scanning. Process and definitions.	4
2.3. Manipulation of DICOM files.	5
2.4. Three dimensional coordinate system. Definitions.	7
2.5. Structures of interest for the study	8
2.6. Evaluation of values obtained	13
2.7. 3D mesh comparison	13
3. RESULTS	14
3.1. Tibial length	14
3.2. Bone weight	14
3.3. Smallest cortical circumference and its location	15
3.4. Smallest medullary canal area and its location	16
3.5. Tibial proximal epiphysis circumference	17
3.6. Angle of proximal epiphysis with medial cortex	18
3.7. Angle between malleolus medialis and medial cortex	18
3.8. Tibial valgus	19
3.9. Tibial torsion: Measured with two different methods	20
3.10. Tibial Plateau Angle, compared to the mechanical axis (TPA)	22
3.11. 3D Mesh Comparison on two sets of bones	22
4. DISCUSSION	25
4.1. Tibial Length	25
4.2. Bone weight	25
4.3. Smallest cortical circumference and its location.	25
4.4. Smallest medullary canal area and its location.	26
4.5. Tibial proximal epiphysis circumference	26
4.6. Angle of proximal epiphysis with medial cortex	26
4.7. Angle between malleolus medialis and medial cortex	26
4.8. Tibial Valgus	27

4.9. Tibial Torsion	27
4.10. Angle of Tibial plateau compared to the mechanical axis, TPA.	27
4.11. 3D Mesh Comparison on two sets of bones	28
4.12. Global evaluation of measurements	28
4.13. Manual measurements vs automated measurements	29
4.14. Custom-made surgical guides/implants vs. statistical shape model prediction	29
4.15. Limitations: what mistakes might have been done and how to overcome them.	30
4.16. Future studies	33
5. CONCLUSION _____	34
6. SUMMARY _____	35

Acknowledgements

Throughout the research, practical work and writing involved in this thesis I have received a great deal of support and assistance.

Firstly, I would like to thank my thesis supervisor, **Dr. Balázs Gerics**, for his interest in the project, his guidance and patience, and for providing cadavers used for the study.

This study was accomplished with the close cooperation and guidance from my foreign supervisor and friend, **Dr. Alexandre Caron**, DVM, DipECVS, EBVS® European specialist in small animal surgery. Your help, guidance and support have been invaluable throughout the process. Thank you for your collaboration when establishing the goals of this thesis. Thank you for sharing with me your passion for this project and for orthopaedic surgery. You provided me with the tools I needed to choose the right direction and successfully complete this project.

Thank you to **Arnaud Destainville** and **Baptiste de la Bernadie**, engineers in biotechnology from Abys Medical. for their precious insight on the use of 3D technologies in the surgical field, and for sharing their knowledge on the matter.

Advices and insights from **Dr. Bill Oxley**, DVM, DipECVS, EBVS® European specialist in small animal surgery, and founder of 3Dvet, were also very welcome and allowed me to push the project to further grounds. I was encouraged by your interest shown in the project and results obtained. You comforted me about the usefulness of the study.

Thank you to my future colleague, **Dr. Alexandre Guillemot**, DVM, DESV, orthopaedic surgery specialist from *Centre Hospitalier Vétérinaire Atlantia* (CHVA), who suggested that I pursue this thesis subject, after I assisted him in a rather complicated feline tibia reconstruction surgery.

I would also like to thank **Dr. Peter Molnar**, DVM, who carried out the CT scanning of all the bones. Thank you for your help, time, and patience.

Lastly, I would also like to thank my father, **Dr. Jean-Claude Jestin**, DVM, for his great involvement and motivation in collecting and cleaning bones.

I would not have been able to complete this study without all of you.

List of abbreviation

2D, 3D	- Two dimensional, Three dimensional
CAD	- Computer aided design
CdC	- Caudal Condylar axis
CdT	- distal Caudal Tibial axis
CnT	- distal Cranial Tibial axis
CT	- Computer tomography
DICOM	- Digital Imaging and Communications in Medicine
Max.	- Maximum
Min.	- Minimum
Nb.	- Number
Prox.	- Proximal
R ²	- Coefficient of determination
SSM	- Statistical shape model
STL	- Stereolithographic file
TPA	- Tibial plateau
vs.	- Versus (against)

All the illustrations and photographs used in this thesis have been created by the author, unless otherwise stated.

1. INTRODUCTION

1.1. Why choose Feline Tibia?

From the surgical point of view, the tibia is one of the most problematic bone in the cat [Schmierer PA., 2019]. It is a long bone of prior interest, which is considered, in the cat, as “straight and uniform across individuals”, by many orthopaedic surgeons [Oxley B, 2019] (low inter-individual variability).

It is common to observe (distal) tibial fracture, which are difficult to reduce, and come with a healing challenge brought by lack of vascularisation. Internal fixation with plate and screws, has become the most commonly used method of fixation. The fracture reduction problematic dwells in the cortical angles observed in the tibia, which are not easily replicated during the (in-surgery) plate contouring, required by this method. Plate contouring inaccuracy leads to imperfect fracture reduction, in turn leading to a longer recovery and possible unwanted joint deviation: valgus, varus, torsional translation, pre- or re-curvatum.

In humans, another species with low inter-individual variability, pre-contoured (i.e. anatomical) plates have been designed and commercialised for years, and are nowadays commonly used [Arthrex, 2014]. Precise determination of feline skeletal “3D shape” could lead to the development of anatomical plates, especially pre-contoured to the feline appendicular bones. Establishing a database referencing those measurements can also help surgeons better understand cat anatomy and plan surgeries accordingly. Ultimately, demonstrating relative tibial similarities across individuals can lead to the comparison of further bones in the cat skeleton, and the possible establishment of an existing “standard” skeleton according to cats of different sizes.

While many studies involving 2D measurements have been carried out on dogs’ skeleton, the information available concerning cats is still scarce [Schmierer PA, 2019]. 3D comparison of the cat’s anatomy has, to my knowledge, not been performed.

1.2. Objectives

This study aims at comparing feline tibiae proportions between each other, using Computer Tomographic (CT) scanning and associated 3D technologies. Goals involve analysing the (1) sizes and (2) angles/geometry, (3) to determine the degree of skeletal similarity and scalability (i.e. the possibility of a bone to fit into another bone’s shape when being scaled up or down in all three dimensions).

1.3. Hypothesis

1. Felines have a rather homogenous body size, weight, and shape across breeds. We therefore project that the variation amplitude of their skeleton is low, and that within one chosen bone (here the tibia), sizes and angles remain within a close range.
2. Bigger breeds such as Maine Coon and Norwegian cats visually keep the same overall body shape. We predict that their skeleton is a scale-up from a medium sized cat. Therefore, sizes are increased and angles are similar. Proportions are kept.

1.4. Reminder of Tibial Anatomy

The tibia articulates proximally with the femur, distally with the talus, and on its lateral side with the fibula. The tibia can be divided into three segments: (1) the three-sided proximal extremity that carries two condyles that articulates with the femur, (2) corpus tibiae, and (3) the distal extremity carrying the cochlea, which articulates with the talus. [Konig HE., 2004]

The proximal extremity of the tibia, relatively flat and triangular, bears various roughening for ligamentous attachments, and presents articular surfaces for the menisci and corresponding femoral condyles. *Condylus lateralis et medialis* are separated by the sagittal, non-articular *eminencia-intercondylaris* with two *tuberculi intercondylaris*. *Area intercondylaris centralis* is the depression situated inbetween both *tuberculi intercondylaris*. *Sulcus extensorius* cuts into *condylus lateralis*. *Tuberositas tibiae* provides insertion for m. quadriceps femoris and parts of mm. biceps femoris and sartorius. Mm. gracilis, semitendinosus and parts of mm. sartorius and biceps femoris, insert on *margo cranialis* (formerly crista tibiae). M. semimembranosus inserts on the caudal part of *condylus medialis*, and the proximal part of m. tibialis inserts on *condylus lateralis*. [Evans HE., De Lahunta A., 2013]

Corpus tibiae is three-sided throughout its proximal half: its cross section is triangular and has a bigger diameter than the essentially quadrilateral or cylindrical distal half. In the cat, contrarily to the dog, tibia and fibula remain separated throughout life [Hudson L., Hamilton W., 2010]. The proximal part of *facies medialis* is described as wide and practically flat. It is largely subcutaneous and rather smooth throughout. *Facies lateralis* is smooth, wide, and concave proximally, flat in the middle, then narrow and convex distally.

In its distal end, the tibia carries the quadrilateral *cochlea tibiae*, which consists of two arciform grooves, separated by an intermediate ridge. The grooves receive the trochlea of the talus. *Incisura semilunaris* is observed caudally. The medial side of the cochlea is enlarged by a bony protuberance: the *malleolus medialis*. The lateral side is in an oblique plane as it progresses caudolaterally, slightly flattened by the fibula. At the distal end of the fibular surface, the small *facies articularis malleoli*, articulates with the distal end of the fibula. No muscles attach to the distal half of the tibia, except for a small portion of m. fibularis brevis on the lateral side.

For the purpose of our study, we concentrate on the overall geometry of the tibia. We measure lengths, angles and shapes, by anchoring ourselves on the main anatomical structures, without paying particular interest to the fibula and muscle attachments.



Figure 1: Right tibia of a Main Coon. Left to right: Cranial, medial, caudal, dorsal, caudal, plantar views. A. Condylus medialis, B. Condylus lateralis, C. sulcus extensorius, D. Margo cranialis (crista tibiae), E. Malleolus lateralis, F. Malleolus medialis, G. Tuberositas tibiae, J. Linea m. poplitei, K. Incisura poplitea, L. Area intercondylaris, M. et N. Tuberculi intercondylaris medialis et lateralis, O. intermediate ridge of the cochlea, P. medial arciform groove of the cochlea, Q. Facies articularis malleoli, Y. Spatium interosseum cruris, and Z. Fibula.

Muscle attachments: 1. lig. patellae, 2. m. quadriceps femoris, 3. m. sartorius, 4. m. gracillis, 5. m. semitendinosus, 6. m. tibialis cranialis, 7. m. biceps femoris, 8. m. tibialis caudalis, 9. m. flexorum digiti medialis, 10. m. flexorum digiti medialis, 11. m. popliteus.

2. MATERIALS AND METHODS

2.1. Bone collection and preparation

Thirty-five pairs of tibiae were provided for this study (15 + 20 cats from France and Hungary, respectively). Fifteen pairs of tibiae were collected by *La Clinique Vétérinaire des Islandais*, France. Half of them were received already cleaned (i.e. soft tissues were removed), while the other half was delivered non-dissected, though disarticulated at the knee and talo-crural joints. Twenty pairs of specimens were obtained through the Department of Anatomy and Histology at the University of Veterinary Medicine, Budapest, Hungary. Cats were amputated at the lumbar area to keep solely the hind quarters in the freezer until the cleaning process. Limbs were dissected and disarticulated at both the knee and talo-crural joints.

The cats' medical history and breeds are unknown (except for two main coons, and three European mixed breed). Individuals used in the study were euthanised for reasons unrelated to this study. Four specimens were excluded due to fractures, bilateral arthrosis or the presence of growing plates. Those visually assessed to be free of injury or orthopaedic disease of the stifle and talo-crural joints were kept for the study. Unilateral (right) tibiae were investigated. Bones are referenced according to geographical origin (France or Hungary), then randomly numbered. For some data comparison, tibiae of larger breeds are evaluated separately to avoid false interpretation.

It was decided to keep only the cleaned bones in order to limit the need for CT scanning sessions, ease positioning on the CT table, and better hygiene in the scanning area. Following dissection, pairs of tibiae were thoroughly cleaned: most soft tissue was removed and bones were submerged into a hot solution of oxygen-based bleaching agent, paired with ionic and non-ionic surfactant. In order to preserve their structures at best, bones were willingly not boiled, though were left submerged for a minimum of 24h. Following dipping, remaining tissue was removed with non-sharp dissection tools. The process was repeated 3 to 4 times until the amount of remaining tissue attached to the bones was evaluated acceptable.

2.2. Computer Tomographic (CT) Scanning. Process and definitions.

CT allows three-dimensional (3D) evaluation of bone morphology and manipulation of shapes, to make sure measurements are taken in the correct imaging plane. This eliminates possible positioning errors made during the acquisition of radiographic images [D'Amico et al., 2011; Barnes et al., 2015].

CT scanning was carried out by Dr. Peter Molnar, at the Small Animal Clinic of the University. The machine and software settings were firstly tested on a single pair of tibiae. Bones were then scanned on two separate dates, in two separate groups of 16, then 17 pairs respectively. A CT/e scanner by GE Medical Systems was used to obtain one-millimeter-thick, contiguous,

transverse/axial slices, with a window width of 300mm centered at 40, and an exposition time of 1000ms. The protocol ‘9.2 Tarsus supine’ was used. Images generated have a resolution of 512x512 pixels [Table 1].

Table 1: Hardware information and software settings for the computer tomographic scanning process. Information contained in the metadata of the DICOM files.

Field Name	Content
Model, Manufacturer	CT/e, GE Medical Systems
Slice thickness	1,0
Data collection diameter	430,00
Protocol name	9.2 Tarsus supine
Spatial resolution	0.4200000
Reconstruction diameter	305.00000
Distance source-to-detector	949.07500
Distance source-to-patient	541.00000
Table height	-47
Rotation direction	CW
Exposition time	1000
X-ray tube current	50
Generator power	7
Row / column	512 / 512
window width	300

CT scanning allows the segmentation¹ of DICOM² images, for the computation of anatomical reconstruction³ into 3D triangular surface models. This latter can be read and manipulated into a variety of open-source or commercially available software programs. These allow mathematical manipulation of bones, as well as distance and angle measurements across planes and matter. Additionally, the ‘Hausdorff distance comparison principle’, commonly used in computer imaging, and newly appearing in the medical imaging field, allows the direct comparison between two 3D meshes by measuring distances between points of two superimposed shapes [Shingal N., 2004].

2.3. Manipulation of DICOM files.

For the purpose of this study, DICOM images obtained were read with several software programs, according to the need to perform measurements in either 2D or 3D spaces. *HorosTM* [The Horos Project, 2018] was used to place markers on DICOM images, which were

-
1. Segmentation (of a CT scan): “In computer vision, process of partitioning a digital image into multiple segments (sets of pixels, also known as image objects)”. [‘Image segmentation’, 2019]
 2. DICOM (Digital Imaging and Communications in Medicine) is a standard for handling, storing, printing, and transmitting information in medical imaging. It includes a file format definition and a network communications protocol.[DICOM library, 2019]
 3. 3D reconstruction: ‘In computer vision, 3D reconstruction is the process of capturing the shape and appearance of real objects.’ [‘3D reconstruction’, 2019]
 4. Area: defined as the space occupied by a flat surface. It is measured in square units. [‘Area’. 2019]

then used to perform 2D measurements: Tibia length, proximal epiphyseal area⁴, minimum cortical circumference, and minimal medullary canal area.

3D measurements firstly required the reconstruction of DICOM images into 3D volumes. This process needs a clean segmentation of bones from the CT slices. Segmentation was originally performed in *HorosTM* with unsatisfying results. Further software research lead to experimenting with the possibilities offered by *3DSlicer*; an advanced open source software, particularly built for 3D reconstruction and manipulation of DICOM files [Fedorov A. et al., 2012]. As the study does not involve contralateral comparison, it was decided to segment and export only the right tibiae. For the purpose of the study, contralateral bones are considered mirrored. Additionally, the fibulae were not isolated from tibiae, since they were thought not to interfere with measurements and isolating them would have made the segmentation more difficult. This was a wise choice, since, later, the *malleolus lateralis* helped evaluating the tarsocrural joint orientation.

Segmentation process: In *3DSlicer*, the DICOM files, each containing 16 and 17 pairs of tibiae, are divided in 16 and 17 segmentation layers respectively. For each bone, a new segment is added and named according to country reference (F for France, H for Hungary) and numbered from 1-15 and 1-18 (i.e. F01 to H18). In the ‘segment editor’ of *3DSlicer*, the ‘Threshold’ tool computes a prior selection of bone matter. A threshold range of -360 to 230, with the *Otsu* protocol is used. Each bone is isolated thanks to the ‘Island’ tool. The segmentation can then be perfected slice and slice, by correcting the area of segmentation with the ‘paint’, ‘draw’ and ‘erase’ tools. The process is repeated for each bone. The quality of segmentation is verified thanks to the in-built 3D visualisation of *3DSlicer*.

Segmented bones are exported to .stl files. An .stl file format stores information about 3D models and is portable across all Computer Aided Design (CAD) software programs. It also allows communication between a computer and a 3D printer. This format describes only the surface geometry of a 3D object, stored as a collection of triangles (or facets), referred as tessellation⁵ [Figure 2] [Chakravorty, 2019]. Stl files allow the transfer, manipulation and evaluation of tibia in more adapted software programs.

Several scientific articles describe the comparison of bones using CT files and 3D reconstructions [Vlachopoulos L. et al., 2018; Smith EJ. et al, 2017; Dunlap AE. et al., 2018]. They do not report using any automated process to register their measurements. The French company *Abys Medical*, working on similar projects in the human field, confessed that, so far, they do not know about an automated method to compare 3D shapes, and that most scientific studies mainly use manual work to collect data. In one study, a novel python-based algorithm was developed for computation of femoral angles [Longo F. et al, 2017]. In the lack of expertise to develop such algorithm, it was decided to evaluate, and list all measures, bone by bone, to then calculate their mean values.

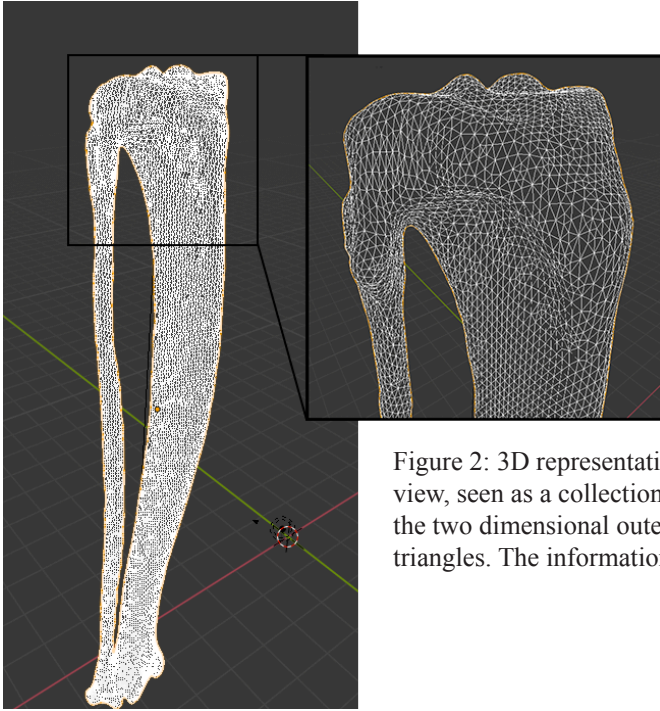


Figure 2: 3D representation of the cat tibia. Cranio-lateral perspective view, seen as a collection of triangles: when converted to stl files, the two dimensional outer surface of 3D models are tessellated using triangles. The information about those triangles are stored within the file.

Blender[®] was used to manipulate and measure tibiae in a 3D environment [The Blender Foundation, 2019], where angles were measured (angle of proximal epiphysis, angle of malleolus medialis, tibia valgus, tibia torsion, tibial plateau angle), and tibial length were double-checked. Later, *CloudCompare*[®] [2019] was used to apply the Hausdorff shape comparison protocol.

2.4. Three dimensional coordinate system. Definitions.

A three-dimensional Cartesian coordinate system consists of three axes that all go through a common point denoted as the Origin, and are mutually perpendicular. Each axis is represented as a single directional vector, and all axis have a single unit of length. The x -, y -, and z -axis vectors define the three coordinate axes. The coordinates of any point in space are determined by three real numbers (x, y, z) . [Svirin A., 2019] [Figure 3].

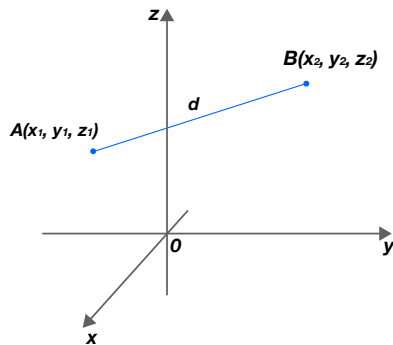


Figure 3: 3D coordinate system having O as its origin. d is the distance between the two points A and B .

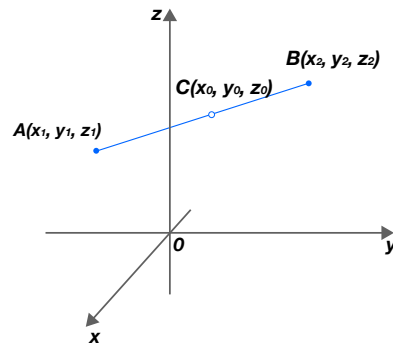


Figure 4: 3D coordinate system illustrating the division of segment $|AB|$ by the point C .

-
5. Tessellation: process of tiling a surface with one or more geometric shapes such that there are no overlaps or gaps. [Chakravorty, 2019]

2.5. Structures of interest for the study

With the aim of getting a global idea of how similar bones are, a list of structures seeming relevant from an anatomical and orthopaedic point of view is established.

- **Tibial length:** Length is measured along the mechanical axis, from the *area intercondylaris centralis*, to the proximal border of the cochlear ridge [Petazzoni M., Jaeger GH., 2008]. Using Horos™, the DICOM files are browsed slice-by-slice to find the above mentioned anatomical landmarks [Figure 6], where reference ‘points’, A and B, are placed [Figure 5]. For any ‘point’ placed on a slice, the full information about its location in the 3D space becomes available. The 3D coordinates of A (x_1, y_1, z_1) and B(x_2, y_2, z_2) are noted, and are used to calculate the tibial length using the mathematical formula: $L = |AB| = [(x_2-x_1)^2+(y_2-y_1)^2+(z_2-z_1)^2]^{1/2}$ [Svirin A., 2019] [Annexe 1].
- **Bone weight:** As we are missing basic information about the relevant cats (age, body weight, race), the bone weight gives us a prior idea of the cats’ size. The weight is assessed with a high precision scale: to the milligram.
- **Smallest bone cortical area width and its location:** Since it is visually impossible to determine which transverse CT slice reveals the smallest cortical area, the bone contour⁶ is traced on each slice with the ‘closed polygon’ tool, in Horos™, in order to determine the smallest value [Figure 6], and its location along the bone length (z axis), which is noted: C(z_0). The coordinate C(z_0) can be demonstrated by the formula: $z_0 = (z_1 + \lambda z_2) / (1 + \lambda)$, where λ is the unknown ratio at which C divides the bone length [Figure 4]. $\lambda = AC / CB$ [Svirin A., 2019]. This translates to $\lambda = (z_1 - z_0)/(z_0 - z_2)$. Together with values of area and contour, λ allows to compare the smallest cortical circumference as a function of the length, to determine whether bones of different size are scalable and/or keep a close ratio across sizes.
- **Smallest medullary canal area and its location:** Area and location of the smallest medullary canal are measured similarly to the smallest bone width.
- **Proximal epiphysis circumference:** Measured at the maximum circumference value on the CT slices: the visually biggest area is contoured with the ‘closed polygon’ tool, in Horos™, and its area is noted [Figure 6]. The proximal epiphysis circumference is used as another reference value to compare proportions as a function of the length.

6. Contour: outline bounding the shape of the bone.

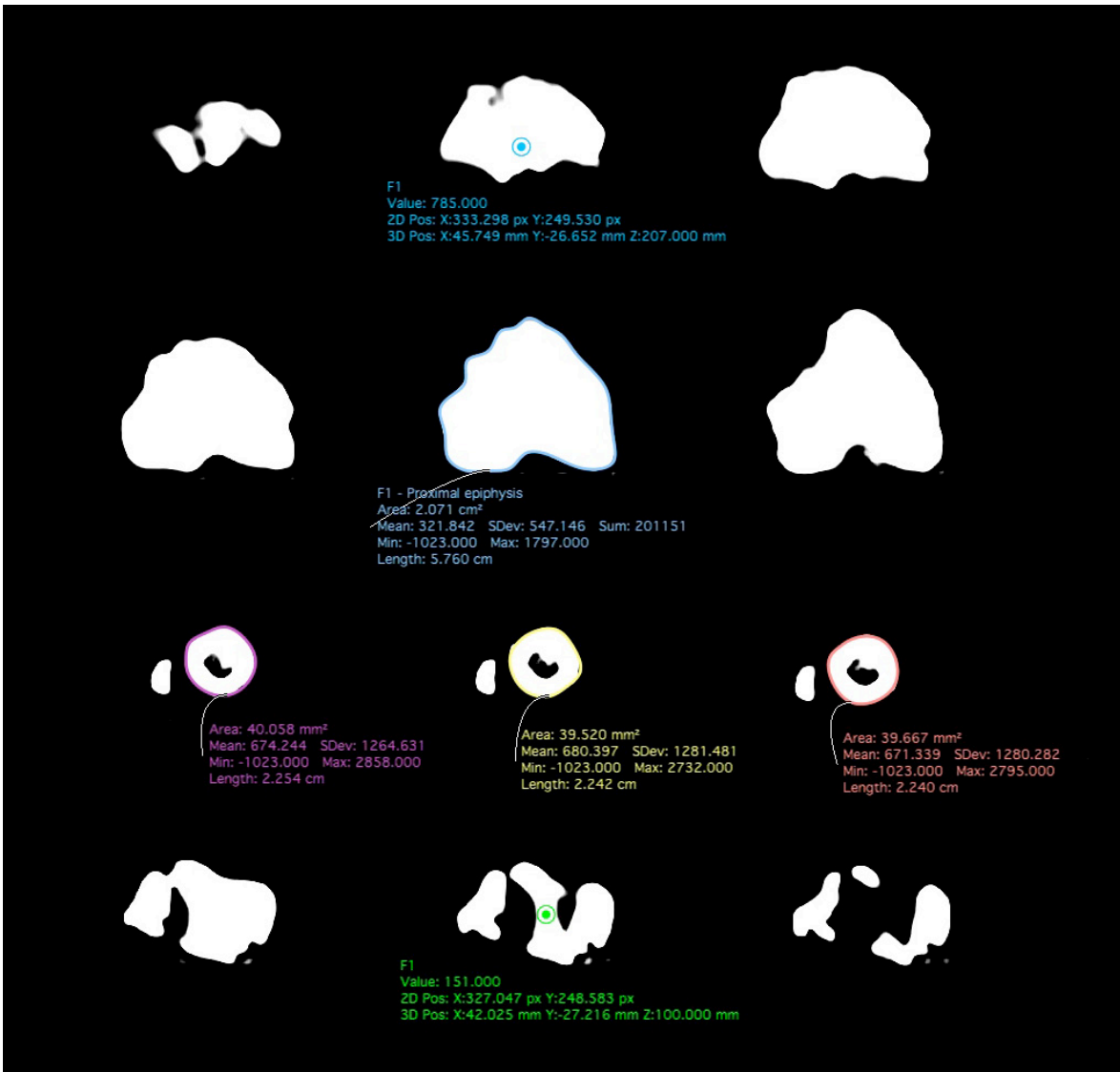
7. Orthographic projection (sometimes referred to as orthogonal projection) is a means of representing three-dimensional objects in two dimensions. It is a form of parallel projection, in which all the projection lines are orthogonal to the projection plane [‘Orthographic projection’, 2019]



Figure 5: (left) 3D representation of a cat tibia in Blender®. (left) orthographic⁷ cranial view, (right) orthographic⁷ lateral view. represented with its mechanical axis in the frontal and sagittal planes. This segment is used to measure the bone length. (A) area intercondylaris centralis (B) Caudal border of the cochlea.

Figure 6: (below) selected CT slices read in Horos™ from the DICOM file. (z) coordinates from left to right: (1) 208, 207, 206. (2) 205, 204, 203. (3) 124, 123, 122. (4) 101, 100, 99.

- (1) First line: The blue point in the area intercondylaris. Its (x, y, z) coordinates are noted for length calculation.
- (2) Second line: Evaluation of the prox. epiphysis circumference. The biggest area is traced.
- (3) Third line: Evaluation of the min. cortical circumference. A few slices are traced. The smallest value is noted.
- (4) Fourth line: the green point is the prox. border of the cochlea. Its coordinates (x, y, z) are noted for length calculation.



- Tibial torsion:** The tibial torsion is defined as the angle between the transverse axes of the proximal and distal tibial articular surfaces. Two techniques are used to evaluate it. The first method, described in the dog by Aper R. et al (2005), consists in measuring the angular relationship between reference lines (axes) on both proximal and distal aspect of the bone: Caudal Condylar axis (CdC), distal Caudal Tibial axis (CdT), distal Cranial Tibial axis (CnT) [Figure 7]. The second method of tibial torsion evaluation was developed after obtaining results from the first method that failed to (1) identify a consistency between the two angles measured, and (2) recognise a relationship between the chosen landmarks and the joint orientation itself. It consists of visually assessing the angle between the femorotibial and tibio-tarsal joints directions. The femorotibial joint direction is materialised by a line placed parallel to both *tuberculi intercondylaris* (FTJo). The Tibio-tarsal joint direction is represented by three lines following the direction of the *cochlea tibiae* (TTJo) [Figure 8].

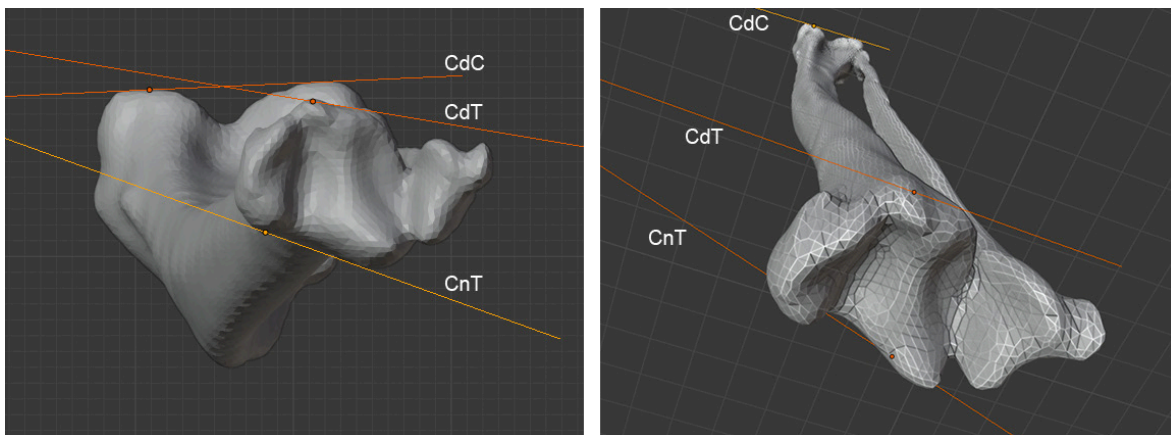


Figure 7: 3D representation of: ventral orthographic⁷ view of the distal articular surface of the cat tibia superimposed over the proximal articular surface (left). Caudo-ventral perspective view (right). Illustration of the first technique used to evaluate the tibial torsion. CdC, Caudal Condylar axis; CdT distal Caudal Tibial axis; CnT, distal Cranial Tibial axis.

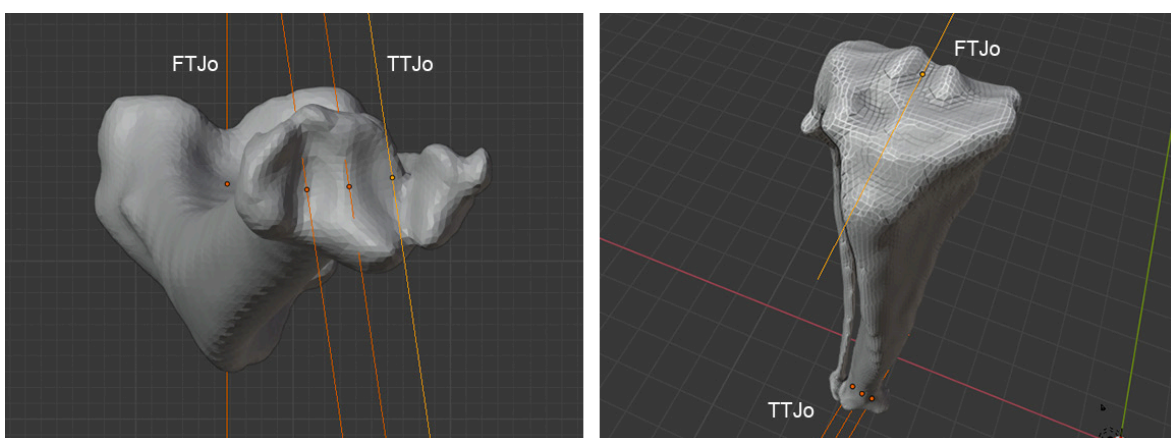


Figure 8: 3D representation of: ventral orthographic view of the distal articular surface of the cat tibia superimposed over the proximal articular surface (left). Cranio-dorsal perspective view (right). Illustration of the second technique used to evaluate the tibial torsion. FTJo, Femorotibial joint orientation; TTJo, Tibio-tarsal joint orientation.

- **Angle of proximal epiphysis with medial cortex:** Using *Blender*[®], two lines are roughly fitted onto the cortical surface of the proximal epiphysis and corpus tibiae. The section at which the cortex forms an angle is located. The centre of rotation of both lines are placed there, superimposing each other. Lines are then perfectly fitted to the cortex of the proximal epiphysis and corpus tibiae respectively. The angle between those two lines is measured in the 3D environment, by placing the ‘angle measurement’ tool over the two lines. The angle is read. [Figure 10]

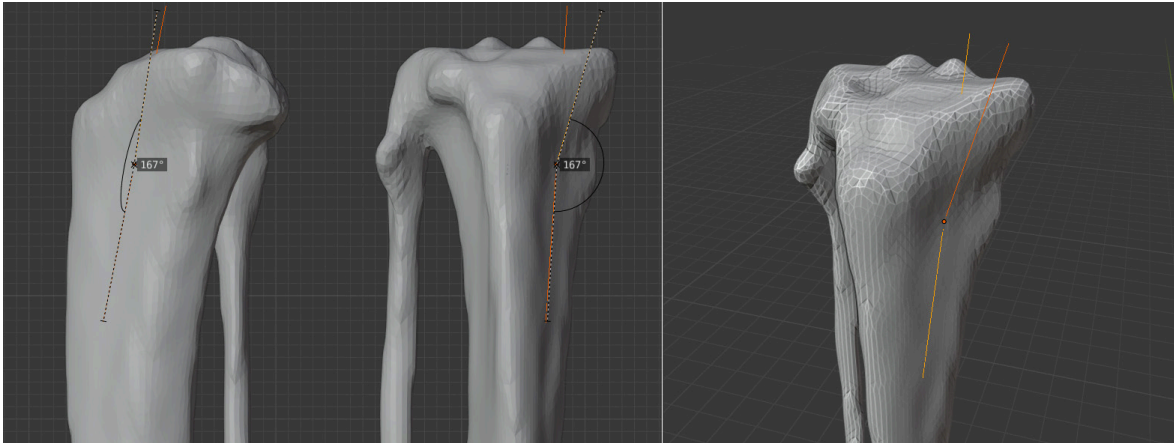


Figure 10: 3D representation of the proximal cat tibia, medial orthographic view (left), cranial orthographic view (middle), medio-cranial perspective view (right). Two segments are used to evaluate the angle between the proximal epiphysis and the proximal bone cortex.

- **Angle between malleolus medialis and medial cortex:** Based on the 3D models of the bones, the curvature forming the malleolus medialis can be illustrated with three straight lines fitting perfectly the most medial bone cortex. Based on mathematical geometry and the triangle angle sum theorem (Pythagorean theorem), this curvature can be defined as the angle between the two outmost lines. [Figure 9]



Figure 9: 3D representation of the distal cat tibia, medial orthographic view (left), cranial orthographic view (middle), medio-cranial perspective view (right). Three segments delimitate the cortex outline. The two outmost are used to measure the angle between the malleolus medialis and the cortex.

- **Tibial Valgus:** Angle measured between the proximal and distal joint orientation lines in the frontal plane [Petazzoni M. et Jaeger GH., 2008]. The proximal joint orientation line, P, passes distally through the concavities of the medial and lateral condyles. The distal joint orientation line, D, is placed centrally and tangential to the most proximal points of the medial and lateral cochlear grooves. 3D shape manipulation is used to make sure the lines are placed to the best fitting positions. [Figure 11]

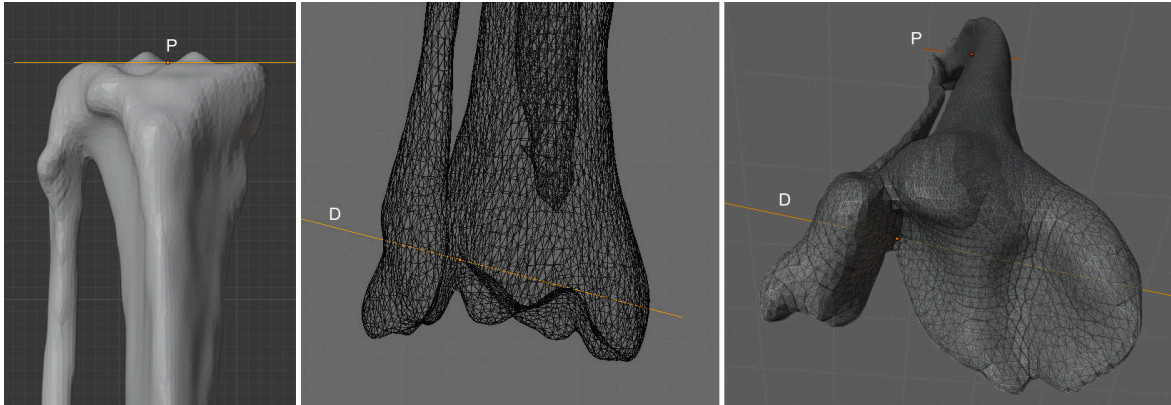


Figure 11: 3D representation of the cat tibia: cranial orthographic view of proximal tibia (left), wireframed cranial orthographic view of distal tibia (middle), distal-cranial perspective view of distal tibia (right). P, Proximal joint orientation line; D, distal joint orientation line.

- **Tibial Plateau Angle, TPA:** In a two-dimensional environment (typically used on X-ray images), the joint orientation line of the proximal tibia, is represented in the sagittal plane by a line passing through the cranial and caudal extents of the tibial plateau. [Petazzoni M. et Jaeger GH., 2008]. In the 3D environment, this line does not fit perfectly the TPA, which has a rather convex shape. The line used to measure the TPA is therefore placed considering both the landmarks established for X-ray imaging and observations made on the 3D shape: placing the line as a tangent to the plateau [Figure 12].

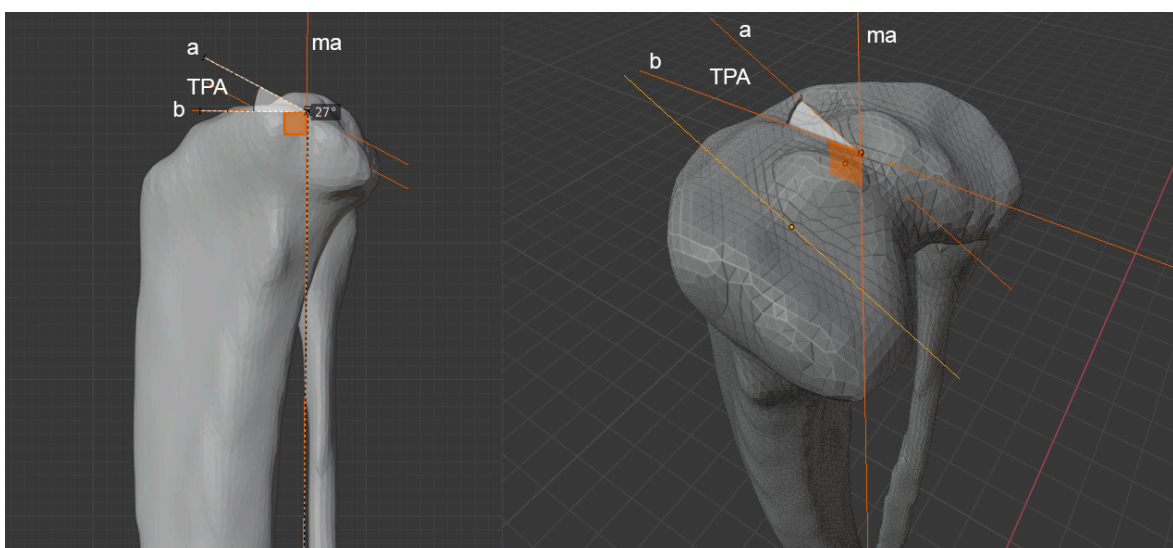


Figure 12: 3D representation of the proximal cat tibia. medial orthographic view of the proximal tibia (left), medio-dorsal view of the tibial plateau (right). TPA, tibial plateau angle; ma, mechanical axis; a, line parallel to the tibial plateau; b, axe perpendicular to the mechanical axis.

2.6. Evaluation of values obtained

For each variable, *Google Sheets*[®] is used to calculate the average value and standard deviation. A low standard deviation indicates that values are close to the mean (expected value), whereas a high standard deviation indicates a spread out over a wider range.

Google Sheets[®] is also used to generate scattered plotting charts, and to draw trendlines that illustrate the coefficient of determination (R^2), which illustrates the “proportion of the variance in the dependent variable that is predictable from the independent variable(s)” [[‘Coefficient of determination’, 2019](#)]. Simply explained, the R^2 value, expressed in percentage, indicates the predictable variability of a value on the Y axis, depending on the X axis variable (For instance, The weight variability can be explained at 65% by the change of length. The remaining 35% is due to unexplained variables [*Figure 14*]). The closer to 100% R^2 is, the higher the predictability.

For some angle measurements, the normal distribution is examined. It is an application of the central limit theorem, stating that averages of observed samples of same origin “converge in distribution to the normal”. The normal distribution is sometimes informally called the “bell curve”. This curve helps us determine the value towards which our measures converge, despite possible error of measurements and individual anatomical anomalies.

2.7. 3D mesh comparison

The mesh processing software *CloudCompare*[®] is used for its shape comparison algorithm, which apply the Hausdorff distance comparison principle between two 3D shapes. The Hausdorff distance measures how far two subsets of a metric space are from each other.

Two comparisons are made. The first one is done between two bones of similar size. The second, between two bones of different sizes. The two chosen bones are loaded into the *CloudCompare*[®] software, and the shapes are registered with a cloud sampling limit of 100,000. This applies a transformation matrix that overlap bones to the lowest possible Hausdorff distance. In the case of bones having different sizes, they are automatically scaled to match each other’s shape to the closest level possible. The scale applied is registered. Then the mesh-to-mesh distances are computed. The distances measured between individual points of 3D meshes are illustrated by colour grading schemes [*Figure 32*] & [*Figure 33*], outlined in a histogram & weilcurve [*Figure 29*]. The algorithm also outputs the mean distance and standard deviation concerning the calculated measures.

3. RESULTS

Individual results are listed on Annex 1.

3.1. Tibial length

Bones of Main Coons and cats of other taller sizes are excluded from the averaged length, though included in the histogram chart [Table 2] & [Figure 13]. Tibiae are considered to belong to taller breeds when longer than 115.5mm. Their average tibia length is 14.3mm longer than standard sized cats [Table 2].

Table 2: Tibial length, measured in millimetres (mm).

Bones origin	French	Hungarian	Total	Large Breeds
Nb. of cats evaluated	12	14	26	4
Average Length	107.73	106.65	107,15	121.45
Longest bone	115.01	114.09	115.01	130.05
Shortest bone	99.05	97.04	97.04	116.04
Standard deviation	4.89	4.62	4.83	5.57

The distribution of tibiae length is illustrated by an histogram chart that shows a larger proportion on bones being between 105mm and 115mm.

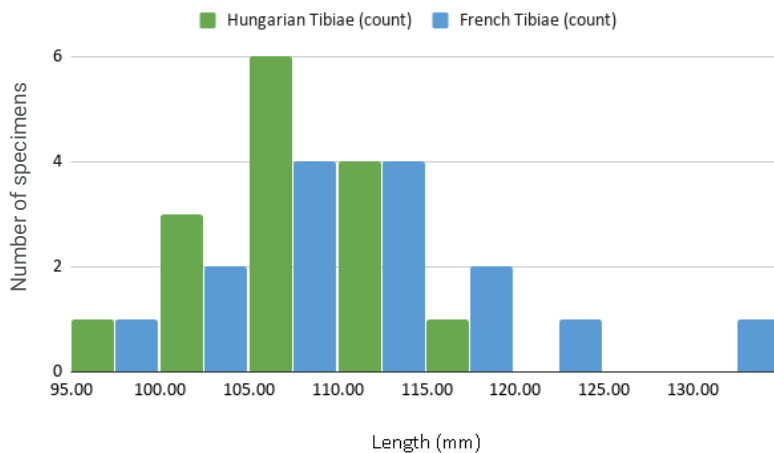


Figure 13: Histogram chart illustrating the distribution of the length value of the bone set.

3.2. Bone weight

Bones of large breeds were excluded from the averaged weight.

Table 3: Tibial weight mean values, measured in grams (g), and separated by country of origin, and size.

Bones origin	French	Hungarian	Total	Large Breeds
Nb of cats evaluated	12	14	26	4
Average weight	9.79	8.44	9.06	13.88
Highest weight	14.43	10.1	14.43	14.72
Smallest weight	6.98	6.7	6.7	13.00
Standard deviation	2.04	0.99	1.73	0.62

The tibia weight is plotted against the length, in order to observe a possible relationship between the two [Figure 14].

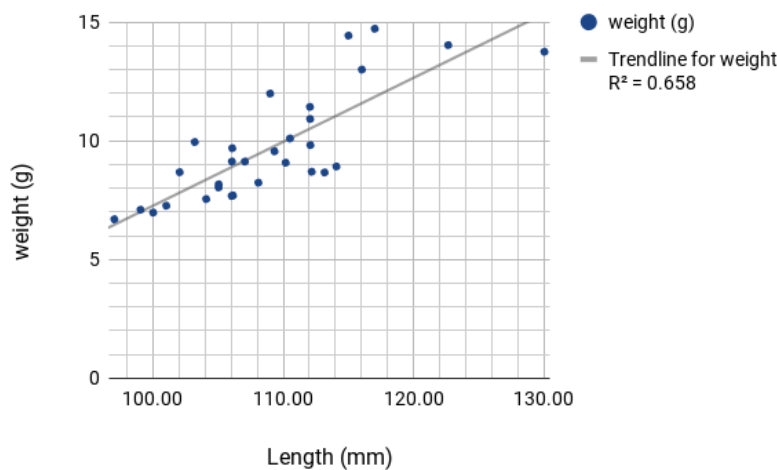


Figure 14: Scattered plotting of relationship between the length of bones and their weight. With linear tendency line having a coefficient of determination, $R^2=0.650$.

3.3. Smallest cortical circumference and its location

Table 4: Smallest cortical circumference and location. The area value is measured in square millimetres (mm^2). The contour is measured in centimetres (cm). The ratio is expressed in percent (%) of the bone length, taking for origin the cochlear ridge.

Bones origin	French	Hungarian	Total	Large Breeds
Nb of cats evaluated	12	14	26	4
Average area	41.77	39.87	40.74	52.51
Biggest area	53.843	46.433	53.843	57.67
Smallest area	32.464	32.753	32.464	48.08
Standard deviation	6.03	3.93	5.18	3.89
Average contour	2.32	2.26	2.28	2.61
Biggest contour	2.639	2.433	2.639	2.70
Smallest contour	2.067	2.058	2.058	2.53
Standard deviation	0.17	0.11	0.14	0.07
Average Ratio value	33.00	29.00	31.00	28
Highest ratio	45.95	65.57	65.57	30
Smallest ratio	15.46	10.64	10.64	25
Standard deviation	9.00	13.00	11.00	2

The smallest cortical circumference values are plotted against the length [Figure 15] in order to observe a possible relationship. Its location is also plotted against the length [Figure 17].

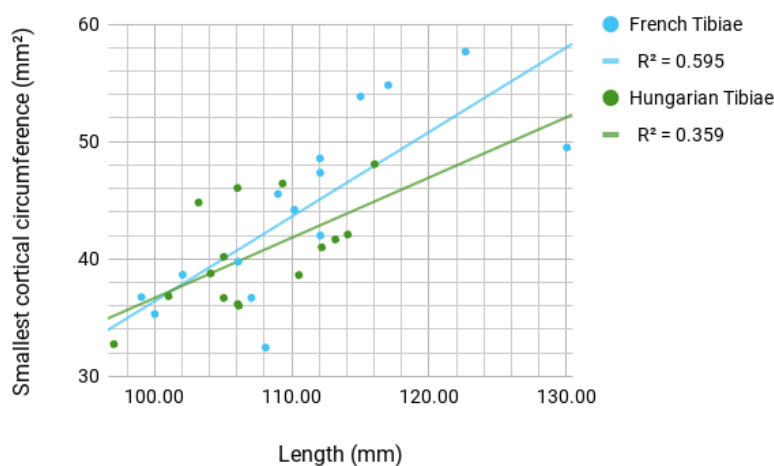


Figure 15: Scattered plotting of length vs. smallest bone circumference. With linear trendline having a R^2 of 59.5% and 35.9% for French and Hungarian bones, respectively.

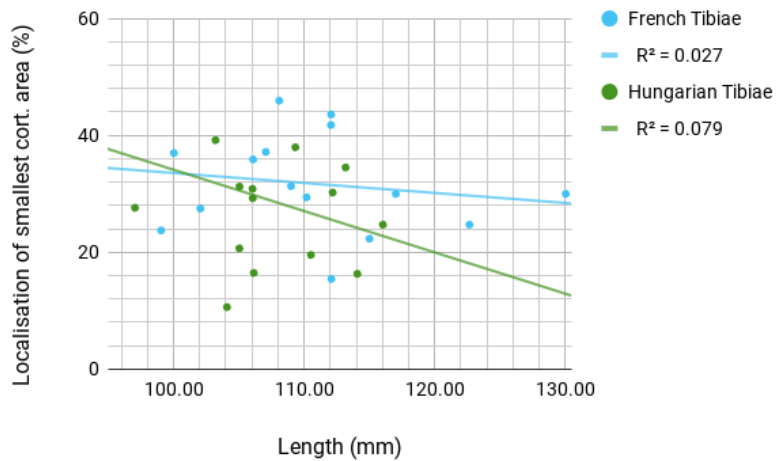


Figure 16: Scattered plotting of length vs. localisation ratio of the min. bone circumference. With a linear trendline having a R^2 of 2,7% and 7% for French and Hungarian bones respectively.

Measurements, carried out manually, allowed to observe that the cortex shape at the location of minimum width is not standard: it varies from almost triangular, to round- shapes to quadrilateral. [Figure 17].

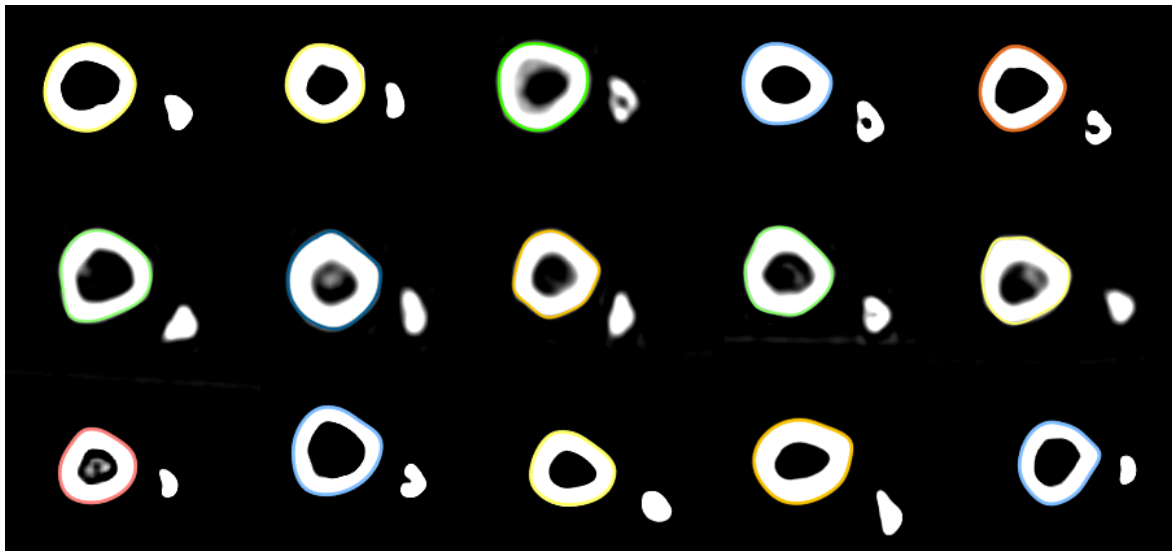


Figure 17: Collection of transverse cuts at the location of smallest cortical circumference, that illustrate morphism between the bones: from almost round shaped to polygonal, due to the continuation of crista tibiae or the start of the malleolus lateralis.

3.4. Smallest medullary canal area and its location

Table 5: Smallest medullary canal area and its location. The area is measured in square millimetres (mm^2). The location ratio is measured in percent of the length of the bone, taking for origin the cochlear groove.

Bones origin	French	Hungarian	Total
Nb of cats evaluated	13	16	29
Average area	10.39	10.60	10.50
Biggest area	21.1180	15.0260	21.1180
Smallest area	1.1430	5.6820	1.1430
Standard deviation	4.69	3.10	4.01

Bones origin	French	Hungarian	Total
Average Ratio value	0.75	0.61	0.68
Highest ratio	0.9690	0.8909	0.9690
Smallest ratio	0.5964	0.2283	0.2283
Standard deviation	0.11	0.16	0.16

The smallest medullary canal area is plotted against the tibia length in order to observe a possible relationship [Figure 18]. Its location is also plotted against the length [Figure 19].

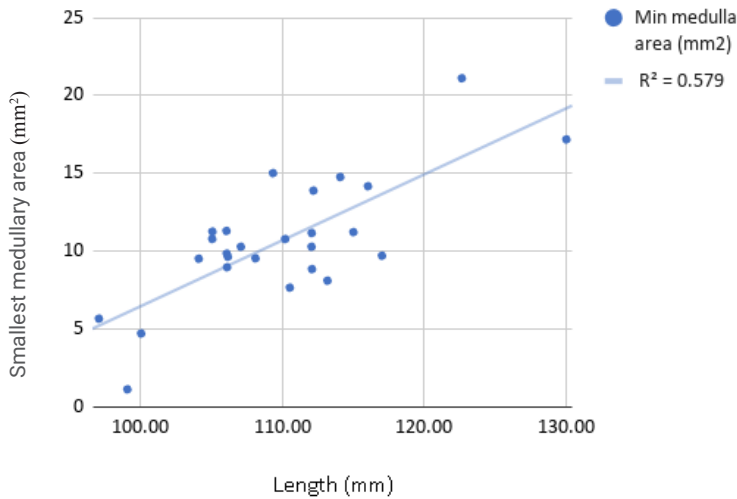


Figure 18: Scattered plotting of length vs. smallest medullary area of the bone, with a linear tendency curve that shows a $R^2 = 57.9\%$

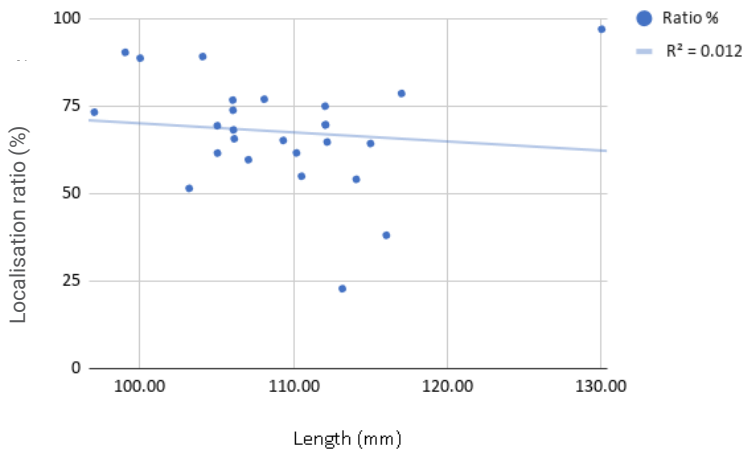


Figure 19: Scattered plotting of length vs. localisation ratio of smallest medullary area of the bone, with linear tendency curve that shows a $R^2 = 1.2\%$

3.5. Tibial proximal epiphysis circumference

Table 6: Tibial proximal epiphysis circumference. Measured as an area expressed in square centimetres (cm²)

Bones origin	French	Hungarian	Total
Nb of cats evaluated	13	11	22
Average area	2.19	2.09	2.15
Biggest area	2.66	2.42	2.66
Smallest area	1.79	1.77	1.77
Standard deviation	0.27	0.19	0.24

The proximal epiphysis of the tibia is plotted against the tibia length in order to observe a possible relationship between the two [Figure 20].

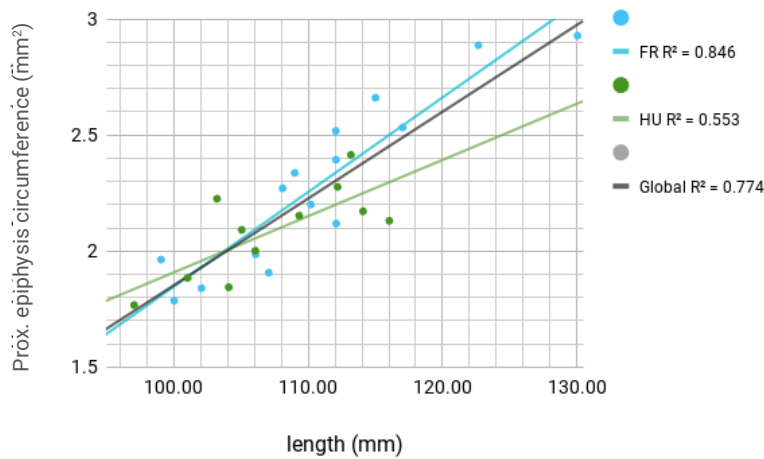


Figure 20: Scattered plotting of length vs. proximal epiphysis circumference. Values separated by country of origin with two different linear tendency curves, which demonstrate coefficients of determination of 84.6% and 55.3%, for French and Hungarian bones respectively. The black linear tendency line represents the global tendency, with a $R^2 = 77.4\%$

3.6. Angle of proximal epiphysis with medial cortex

Table 7: Angle between the proximal epiphysis and medial cortex, expressed in degree angle (°).

Bones origin	French	Hungarian	Total
Nb of cats evaluated	15	16	31
Average angle	165.60	161.88	163.68
Widest angle	170	168	170
Smallest angle	159	150	150
Standard deviation	2.82	4.12	4.01

The angle of the proximal epiphysis with the medial cortex is plotted against the tibia length in order to observe a possible relationship between the two [Figure 21].

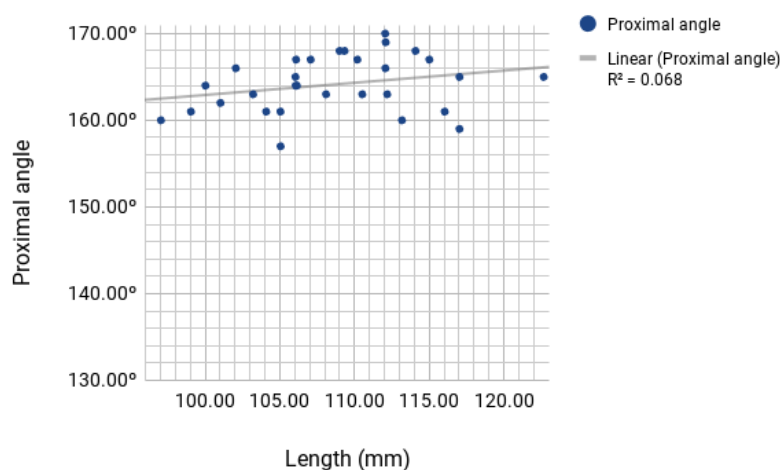


Figure 21: Scattered plotting of length vs. angle between proximal epiphysis & proximal cortex. Relationship illustrated by linear trendline and a R^2 of 6.8%.

3.7. Angle between malleolus medialis and medial cortex

Table 8: Angle between malleolus medialis and the distal medial cortex, expressed in degree angle (°).

Bones origin	French	Hungarian	Total
Nb of cats evaluated	15	16	31
Average angle	157.13	157.13	157.13
Widest angle	165	162	165
Smallest angle	149	144	144
Standard deviation	4.22	4.11	4.16

The angle between malleolus medialis and the medial cortex is plotted against the tibia length in order to observe a possible relationship between the two [Figure 22].

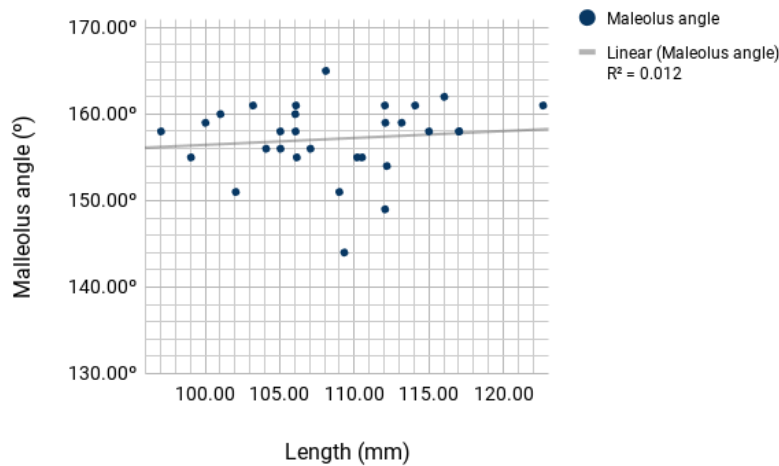


Figure 22: Scattered plotting of length vs. angle between malleolus medialis & distal cortex. illustrated by a linear trendline and a R^2 of 1,2%.

3.8. Tibial valgus

Table 9: Tibial valgus, expressed in degree angle (°).

Bones origin	French	Hungarian	Total
Nb of cats evaluated	15	16	31
Average angle	14.15	18.73	16.51
Widest angle	20.00	27.80	27.80
Smallest angle	7.60	12.50	7.60
Standard deviation	3.60	3.93	4.41

The Tibial valgus is plotted against the tibia length [Figure 23], and against the angle measure between the malleolus medialis and tibial cortex [Figure 24], in order to observe a possible relationship between values.

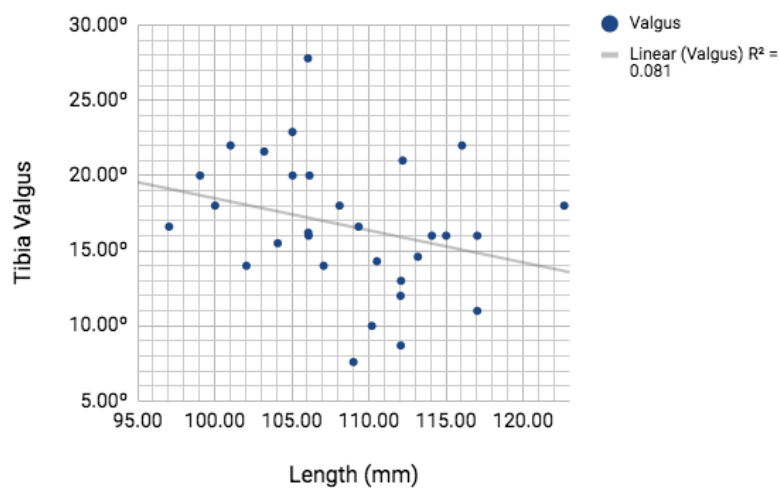


Figure 23: Scattered plotting of length vs. valgus. illustrated by a linear trendline and a R^2 of 0.1%.

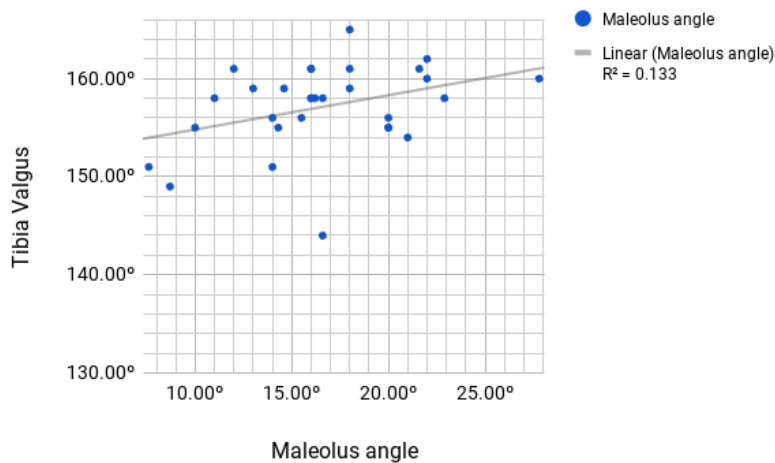


Figure 24: Scattered plotting of the angle between malleolus medialis & cortex vs. tibial valgus. illustrated by a linear trendline and a R2 of 13.3%.

3.9. Tibial torsion: Measured with two different methods

Table 10: Tibial torsion measurement, expressed in degree angle (°).

Bones origin	French	Hungarian	Total
Nb of cats evaluated	15	16	31
Mean CdC-CdT angle	12.36	12.37	12.37
Biggest angle	22.00	37.60	37.60
Smallest angle	-13.00	0.00	-13.00
Standard deviation	8.97	8.95	8.96
Mean CdC-CnT angle	12.91	12.19	12.54
Biggest angle	26.00	21.70	26.00
Smallest angle	2.00	6.40	2.00
Standard deviation	6.72	4.73	5.79
Mean visual angle	10.36	6.86	8.55
Highest angle	17.00	14.00	17.00
Smallest angle	0.40	0.00	0.00
Standard deviation	4.39	3.94	4.52

The various tibial torsion values measured are plotted against each other in order to observe their relationship and potential misleading results. First, CdT-CdC angles and plotted against CnT-CdC angles [Figure 25]. Then, the two latter values are plotted against values registered

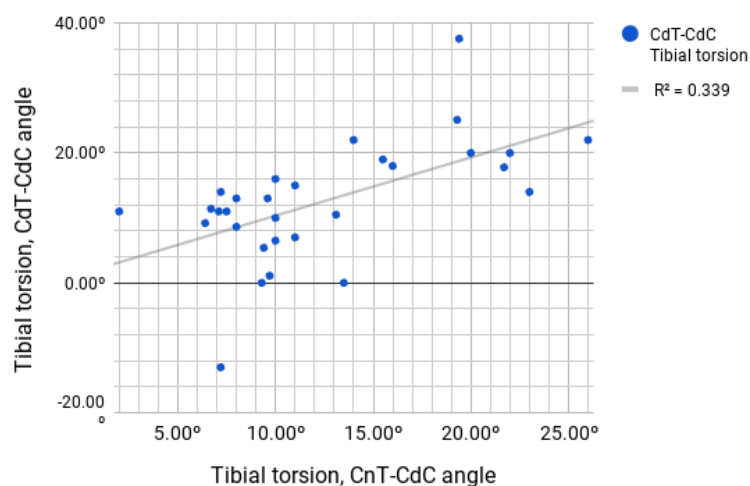


Figure 25: Scattered plotting of angles measured between CnT-CdC and CdT- CdC, illustrated by a linear trendline and a R2 of 33.9%.

with the visually method [Figure 26]. The visually assessed values are plotted against the bone length [Figure 27], and finally, against the minimum bone circumference [Figure 28].

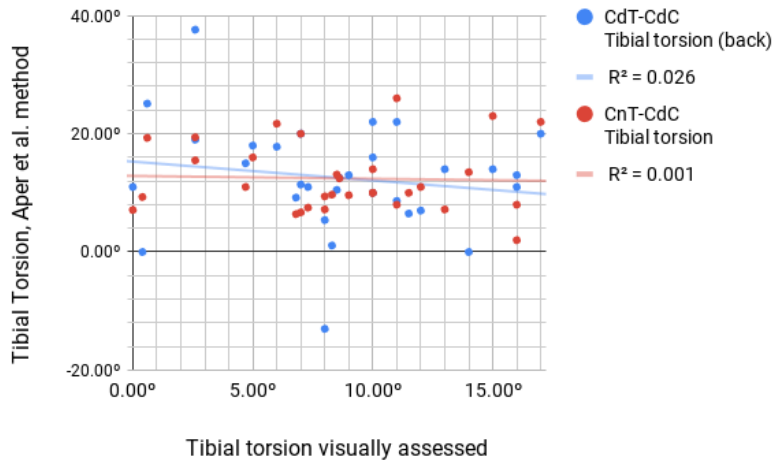


Figure 26: Scattered plotting of visually assessed tibial torsion angle against CdT-CdC and CnT-CdC angles.

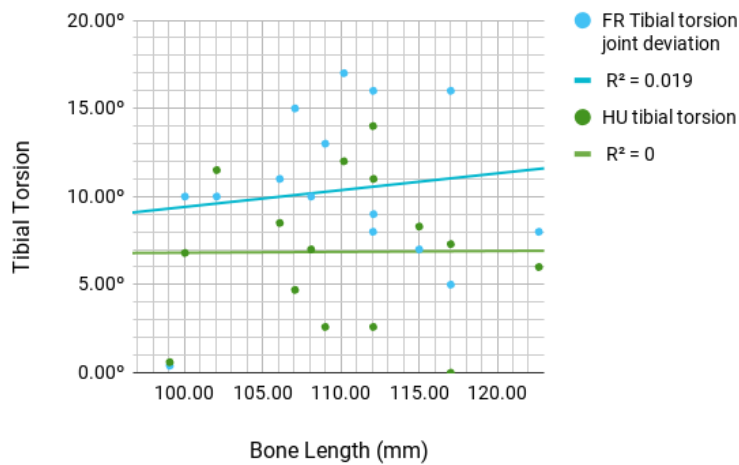


Figure 27: Scattered plotting of the bone length, against the visually assessed tibial torsion angles. Illustrated by linear trendlines having $R^2 = 1,9\%$ and 0% for French and Hungarian tibiae, respectively.

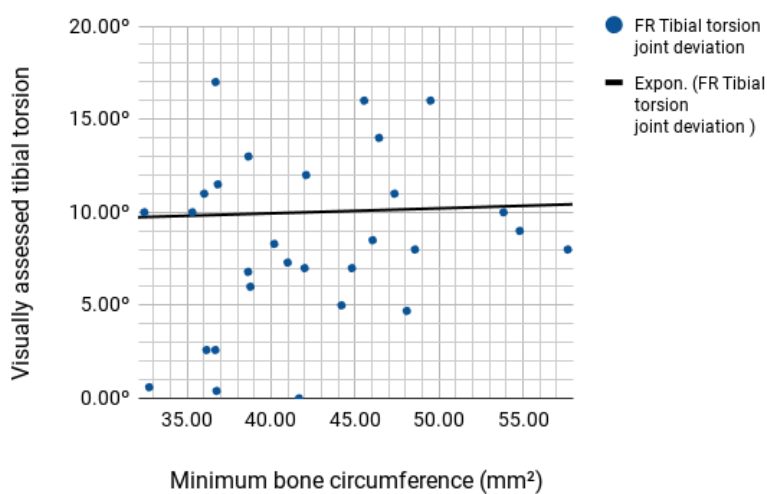


Figure 28: Scattered plotting of visually assessed tibial torsion angle, against the minimum bone width.

3.10. Tibial Plateau Angle, compared to the mechanical axis (TPA)

Table 11: Angle between the tibial plateau and the bone mechanical axis, expressed in degree angle (°).

Bones origin	French	Hungarian	Total
Nb of cats evaluated	15	16	31
Average angle	28.07	32.44	30.32
Widest angle	31	35	35
Smallest angle	25	30	25
Standard deviation	1.57	1.32	2.62

Values of the tibial plateau angle compared to the mechanical axis are placed onto an histogram chart in order to observe their distribution.

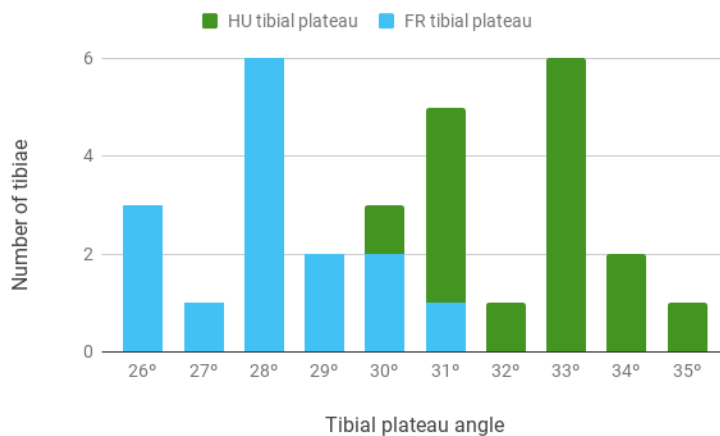


Figure 31: Histogram chart of Tibial plateau angles, representing the number of tibiae found to have a given tibial plateau angle.

3.11. 3D Mesh Comparison on two sets of bones

The first comparison is made between F08 and F11, having a length of 112.07mm and 112.06mm respectively. The colour scale from blue to red illustrate the distance between the two shapes [Figure 32]. Blue signifies a negative distance difference, red signifies a positive distance (blue = crater, negative; red = bump, positive). The colour scale from blue to green illustrates the Hausdorff distance in term of absolute values [Figure 33], which reveals areas where differences are the most pronounced.

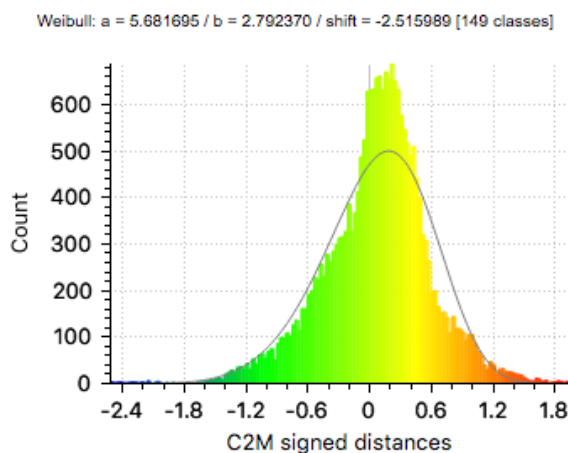


Figure 29: Histogram chart of distance difference distribution between F08 and F11. The Weibull curve illustrates a normal ~ 0.2 mm.

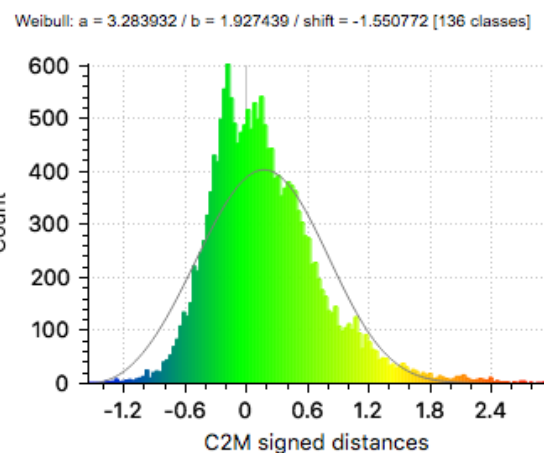


Figure 30: Histogram chart of distance difference distribution between F01 and F04. The Weibull curve illustrates a normal ~ 0.2 mm.

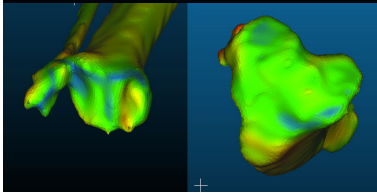
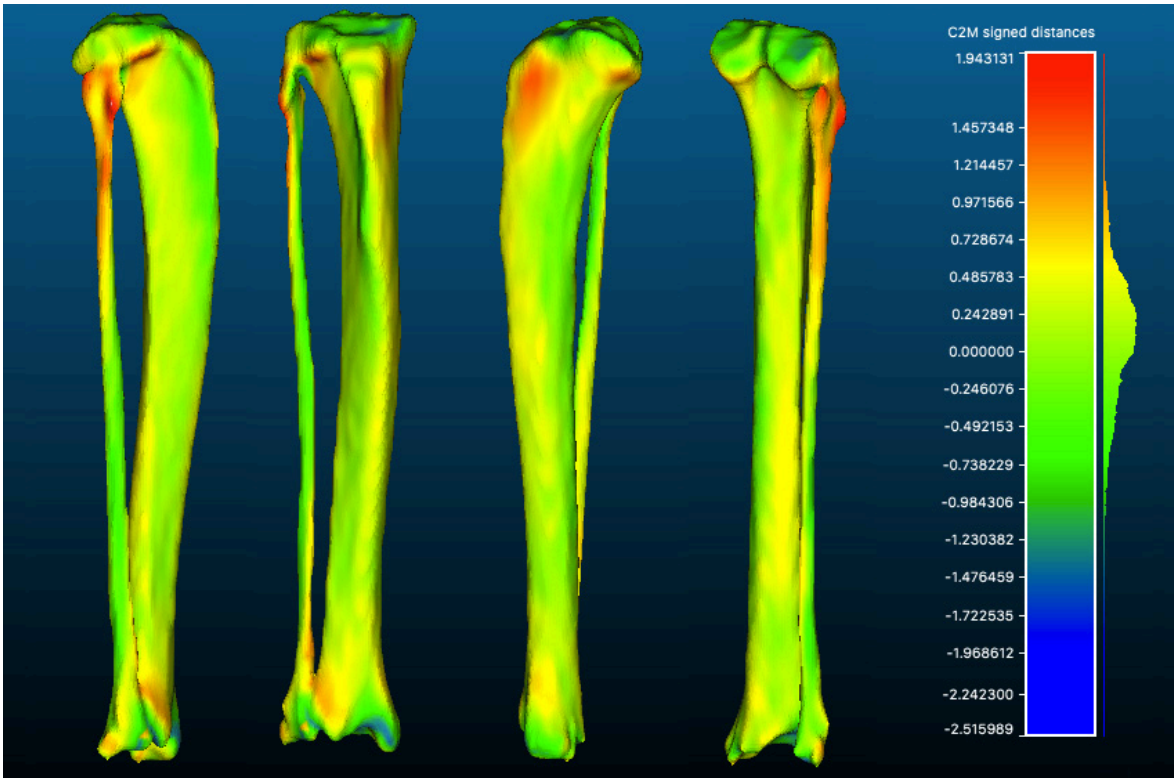


Figure 32: Colour scale from blue to red, computed by the Hausdorff distance algorithm, illustrating the difference between F08 & F11, being about the same length. negative and positive distances are taken into account.

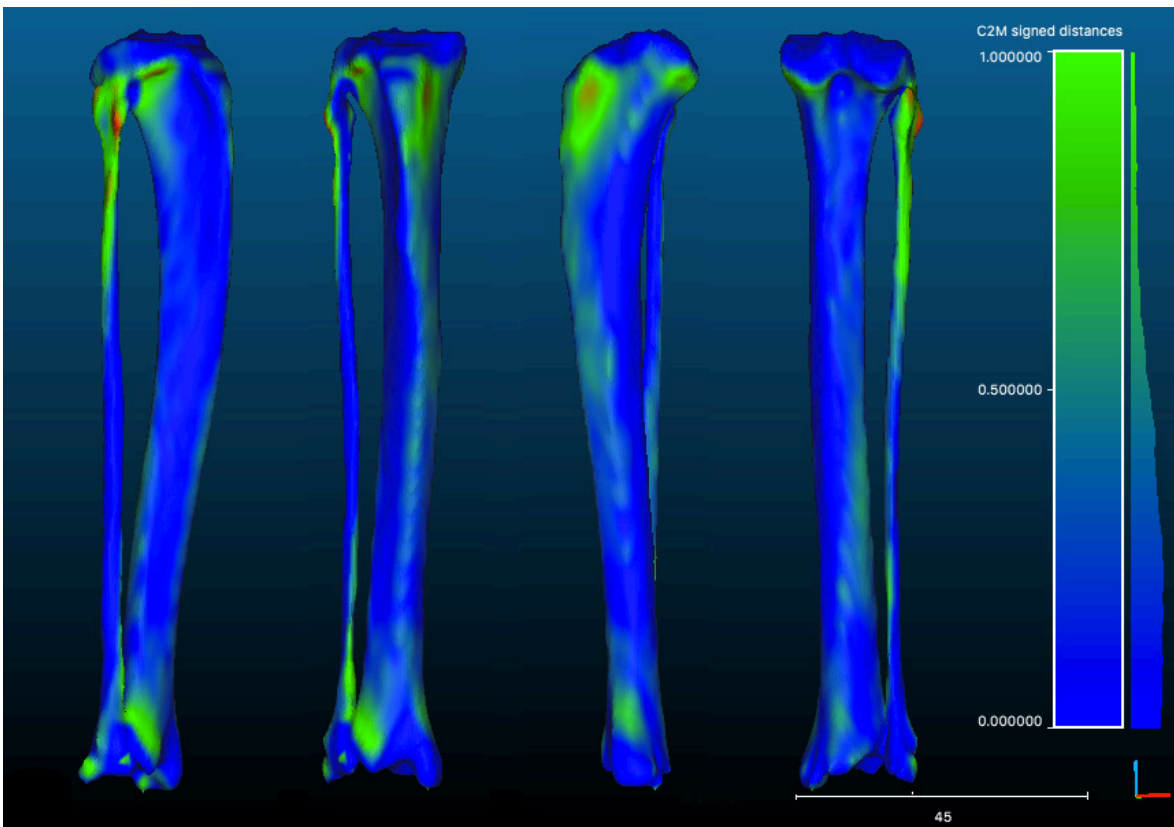


Figure 33: Colour scale from blue to green, computed by the Hausdorff distance algorithm, illustrating the difference between F08 & F11, being about the same length. Here distance are consider in terms of absolute value.

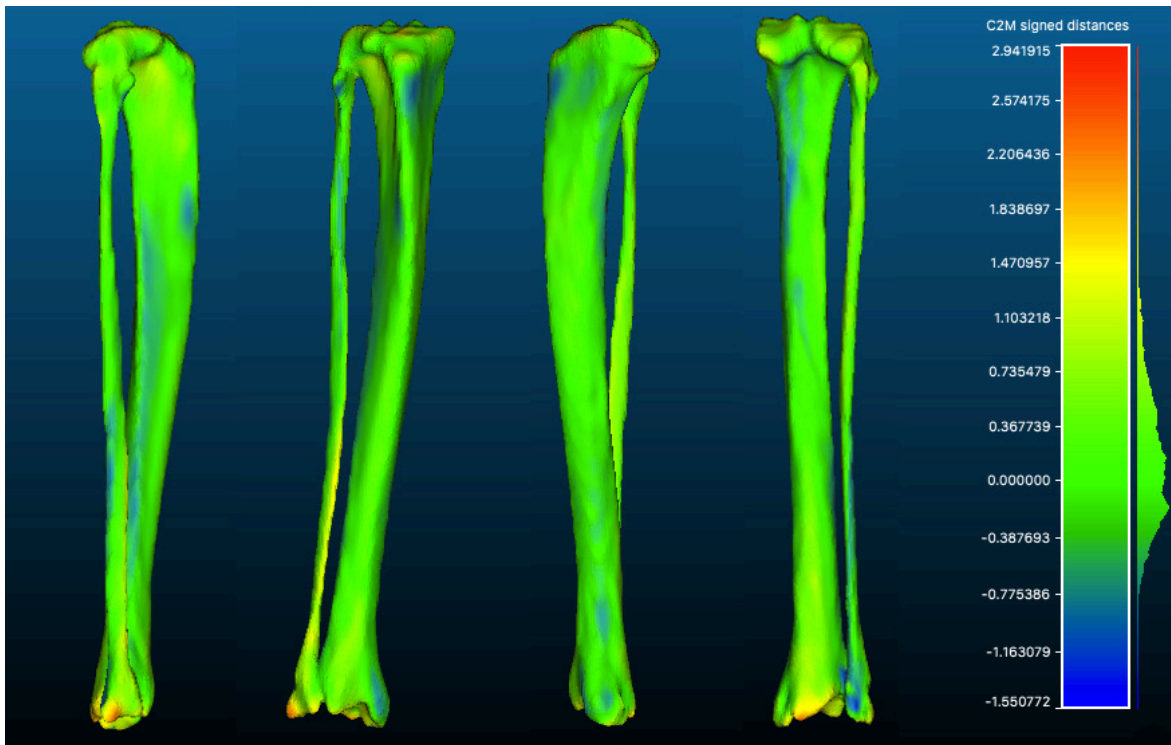


Figure 34: Colour scale from blue to red, computed by the Hausdorff distance algorithm, illustrating the variation between F01 & F04, of different length. Negative and positive distances are taken into account.

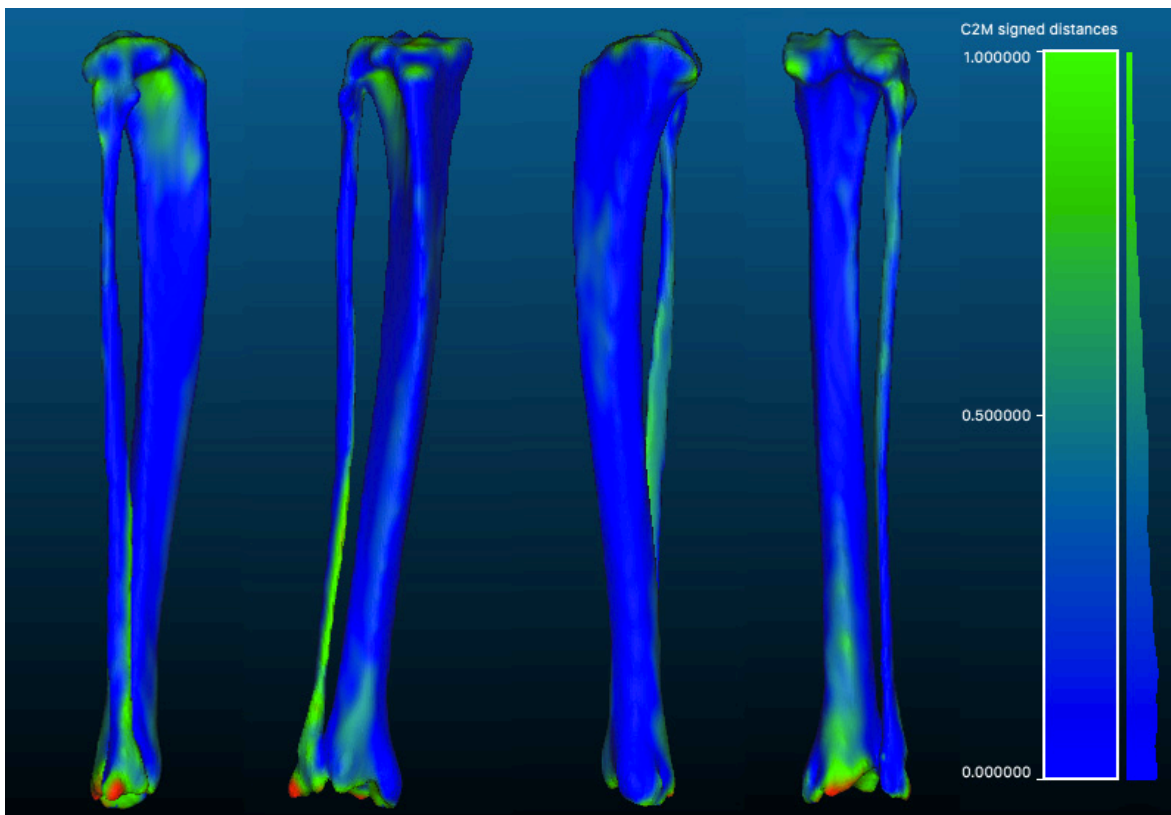


Figure 35: Colour scale from blue to green, computed by the Hausdorff distance algorithm, illustrating the variation between F01 & F04, of rather different length. Distances are consider in terms of absolute values.

The second comparison is made between the randomly chosen F01 and F04, which have a length of 107.07mm and 112.09mm respectively. The scale applied by the software to match the size difference, and apply best superposition equals 0.949181.

4. DISCUSSION

4.1. Tibial Length

In the group of cats of standard size, we observe a larger proportion of tibiae situated between 105mm and 115mm, with a standard deviation of under 5mm, both in the French and Hungarian groups [Figure 13]. We can therefore consider that values of length are kept within a close range. However, deviations in the taller breeds are higher, and we can consider that the taller the breed, the higher the deviation of skeletal size.

In lack of further basic information about the cats (age, weight, breed, withers height), the tibial length becomes the reference value to compare bones to each other. It is assumed equivalent to the withers height of the live cat, and is used to be plotted against other variables.

4.2. Bone weight

By itself, the weight value does not bring any useful information. We plot it against the length, to observe the tendency of their relationship. The general tendency is for the weight to increase together with the general size of the bone [Figure 14].

The coefficient of determination ($R^2 = 65\%$) reveals that a large part of the weight value variability cannot be predicted by the sole change of length. That being said, we know that a margin of error needs to be considered due to the method of cleaning: the will to preserve the bone structure through a low-agressivity cleaning method also lead to the conservation of bone marrow in the shaft of some bones. On other bones, dried tissue remains attached. Moreover, variations observed can also origin from the (unknown) age difference between individuals, due to differences in mineralisation: an older cat has higher chances to have a more porous and therefore lighter bone [Demontiero O. et al, 2012]. All these reasons could explain the lack of higher correlation between tibial length and weight. This is why it was decided not to use bone weight as a reference measurement to compare bones.

4.3. Smallest cortical circumference and its location.

Considering the small scale of the tibial bone cortical circumference, and according to the standard deviation calculated, values found are not considered homogenous. Then, the scattered plotting of the smallest cortical circumference against the bone length, gives a low coefficient of determination ($R^2 = 59,5\%$ and $35,9\%$ for French and Hungarian respectively) [Figure 15]. Furthermore, the scattered plotting of the localisation ratio against the bone length gives an anarchic pattern, with R^2 values brushing against 0% values [Figure 16].

Additionally, we observe a morphism at the location of the smallest circumference, most likely translating to the position along the tibia: continuation of crista tibiae, or start of malleolus [Figure 17]. We therefore conclude that, according to our findings, values of the smallest cortical circumference, and its location along the bone, do not follow a particular fashion. We can therefore conclude that, in this respect, bones are not scalable.

4.4. Smallest medullary canal area and its location.

Similarly to the above mentioned smallest cortical circumference, the smallest medullary canal area, and its location along the bones, do not demonstrate a clear anatomy logic across different bone sizes [Figure 18]. It is particularly clear with the localisation ratio coefficient of determination displaying a value close to 0% [Figure 19], meaning that the length is not at all a determination factor for the localisation variability of the smallest medullary area.

4.5. Tibial proximal epiphysis circumference

Characterised as the widest width of the bone, the proximal epiphysis circumference was generally measured 2mm under the area intercondylaris. Its value tends to increase together with the bone length, at a different rate in each group of bones: the proximal epiphysis circumference increases less frankly in Hungarian bones compared to French ones, and the French values are more closely related to the tendency linear curve [Figure 20]. The R^2 of French bones is also quite elevated compared to the Hungarian one. This is a surprising result considering that the standard deviation is higher in the French group compared to the Hungarian group [Table 6]. In spite of the lack of consistency between the two different groups, there is still a pattern for the proximal epiphysis to adapt to the bone length. This variable can therefore be considered scalable according to the bone length.

4.6. Angle of proximal epiphysis with medial cortex

The angle between the proximal epiphysis and the medial cortex of all bones stay within a closed range, with a mean value of 163.68° , and a standard deviation of 4.01° . French bones have a lesser standard deviation (2.82°) compared to Hungarian bones (4.12°) [Table 7]. The scattered plotting of this angle against the length, coupled with a $R^2 = 6.8\%$, confirms the nearly-absent correlation between the two [Figure 21].

4.7. Angle between malleolus medialis and medial cortex

Similarly to the previously mentioned proximal angle, the angle measured between the malleolus and medial cortex stays within a closed margin, with a standard deviation of 4.16° , and an interestingly constant average value of 157.13° in both groups [Table 8]. The bigger deviation displayed in some individuals give a more dispersed appearance of the scattered

plotting [Figure 22], when compared to the previously mentioned proximal angle [Figure 20]. The R^2 of 1,2% is a clear indicator that the length of the bone has no influence on the value of this angle.

4.8. Tibial Valgus

Once again, the angle of tibial valgus has a standard deviation close to 4° [Table 9], and the R^2 of 8.1% confirms, that the bone length does not have an influence despite a slight tendency to straighten as the bone lengthen [Figure 23]. However, when plotted against the angle measured between malleolus medialis and distal tibial cortex, a trend is observed where the valgus increases with the malleolus angle [Figure 24]. Despite the low R^2 , it does make sense that, together with an increasing joint line, a probable valgus deformation of the entire distal tibia happens, and brings the malleolus with it.

4.9. Tibial Torsion

The tibial torsion measurement method described by ‘Aper et al.’ [“2.5. Structures of interest for the study”, p.8], fails to demonstrate any logic as per the relationship to the torsion itself: the scattered plotting of the CdT-CdC vs. CnT-CdC values seems highly variable: values do not demonstrate a codependency [Figure 25]. By direct observation, we fail to gauge a relationship between both angle measurements described, and the actual rotation of the tibiotarsal joint compared to the femorotibial joint. This assessment leads to disregard those values and to perform the evaluation of the joint angle in a more functional, novel way, by relying solely on joint orientation lines. When plotting the new obtained angle values to the previously measured ones, we again fail to establish a relationship [Figure 26].

Angles identified visually reveal a completely dispersed collection of values. We try to find a possible dependence to the length [Figure 27], or to the smallest cortical circumference of the bone [Figure 28]. With a coefficient of determination close to zero, it is concluded that the tibial torsion does not have a relationship with the previously measured values.

4.10. Angle of Tibial plateau compared to the mechanical axis, TPA.

The tibial plateau angles measured on all 30 bones were found within a closed range, varying by only a few degrees angle. It is to be noted that both French and Hungarian groups show a low standard deviation of 1.57° and 1.32° respectively [Table 11] and a constant higher value is observed in Hungarian cats ($32,44^\circ$) compared to French ones (28.07°) [Figure 31]. Since all values are kept within such a closed range, no relationship with other variables is considered.

4.11. 3D Mesh Comparison on two sets of bones

The coloured maps rendered by *CloudCompare*[®] to illustrate the shapes variations between F08 and F11, point out that the biggest differences between those two bones are situated on the medial tibial tuberosity, sulcus extensorius, and in the cochlea region [Figure 32] & [Figure 33]. The histogram chart outputs a Weibull curves which shows a normal value of ~0.2mm [Figure 29]. Additionally, the program computed a mean distance of 0.07637mm and a standard deviation = 0.53697mm. Those results show a significant similarity between F08 and F11.

The coloured maps of the second comparison, made between F01 and F04, reveal that the biggest differences are situated on the proximal articular surfaces, at the point of insertion of m. tibialis cranialis, and at the malleolus medialis. Overall however, the colour scheme indicates a general resemblance between the two bones after re-scaling. The software also computed a mean distance of 0.184257mm and standard deviation of 0.540318mm. And, once again, the generated histogram shows a normal value of ~0.2mm.

These two 3D mesh comparison demonstrate a high similarity between, on the one hand, two bones of similar sizes and on the other hand, two bones of different sizes. This demonstrates the possibility for (some) bones to be scalable and to retain the same shape independently of their respective size.

4.12. Global evaluation of measurements

Based on our two-dimensional, manually taken measurements, dimensions are found to have a probable link to the bone length (i.e. weight [Figure 14], smallest cortical circumference [Figure 15], proximal epiphysis circumference [Figure 20]), although this relationship is characterised by low-to-average coefficients of determination (65%, 59.5% (for French individuals), and 77.4% respectively), and is not proven clearly. In many of the scattered plottings, it can be observed that bones of similar length, are not similar regarding other, further parameters. It is therefore unclear whether cats have a more or less uniform skeleton with scalable variables, or possess quite different individual designs when it comes to these details. On the other hand, angles measurements are found somewhat independent from other dimensions, and most results are kept within a closed range. Data for the angle between proximal epiphysis and cortex are: $163.68^\circ, \pm 4.01$ [Table 7]; for the angle between malleolus medialis and cortex are: $157.13^\circ, \pm 4.16$ [Table 8]; and for the tibial plateau angle compared to the bone's mechanical axis (TPA) are: $30.32^\circ, \pm 2.62$ [Table 11]. These suggest a continuous similarity across individuals. Moreover, the 3D mesh comparison performed with *CloudCompare*[®] indicates a high similarity between bones of next-to-identical length [Figure 32] & [Figure 33], as well as different length [Figure 34] & [Figure 35].

Based on these results, the creation of a standard bone model for surgical planning is a possibility, as well as the design of a pre-contoured feline tibial plate (with multiple lengths) for medial application, requiring only little adjustment. The project would however require a deeper analysis of the bone shape, especially of the medial border, which is commonly used to apply bone plates.

4.13. Manual measurements vs automated measurements

The mean tibial plateau angle, TPA, found in our study (28.07° in French, 32.44° in Hungarian, 30.32° in both populations combined) is ~5° higher compared to the study conducted by Langley-Hobbs SJ. (2019), who found a mean value of 24° but with a much wider range (13-33°) compared to our population. A further clinical study conducted on 11 cats found a mean TPA of 27° [Mindner JK, et al, 2016]. This difference could either be due to a difference in the population, as demonstrated by our results, or due to measurement methods. The use of universal automated measurements could confirm or refute the existence of such differences.

A 3D Python-based algorithm, using computer-aided design software, was developed with the aim to compare manual and automated methods of measuring femoral angles in the dog. The automated protocol was found the most repeatable and reproducible method when compared to manual radiographic and CT measurements [Longo F. et al, 2017]. This proves that an automated method reduces the margin of error that can be done with manual work. A computed process also provides a morphometric assessment of the bone studied, without the need to manually determine landmarks, and provides an obvious reduction of the time needed to evaluate these angles in clinical cases. [Longo F. et al, 2017]

In our study, all measurements have been made manually, thus inter- and intraobserver variability has to be considered. Developing an automated process would allow more precise measurements and possibly allow to survey a much wider population.

4.14. Custom-made surgical guides/implants vs. statistical shape model prediction

CT imaging, associated to 3D reconstruction and 3D printing has been gaining grounds in veterinary orthopaedic pre-operative planning. Individual patient-based applications multiply with the surgeon's expertise and imagination. A trending practice involves printing the fractured bone for pre-operative plate contouring, allowing a more precise fracture reduction and shorter operative time [Marcellin-Little DJ, 2019]. A further application is using computer-aided design and 3D modelisation, to help correcting skeletal malformations or degenerations, by designing patient-specific surgery-aiding tools (cutting, drilling guides) [Figure 36] [Oxley B., 2019; Hamilton-Bennet S., et al, 2017]. More recently, the first custom-designed titanium implant was developed from the contralateral bone, to replace part of a radius from a dog suffering from osteosarcoma [Creadditive, 2019].

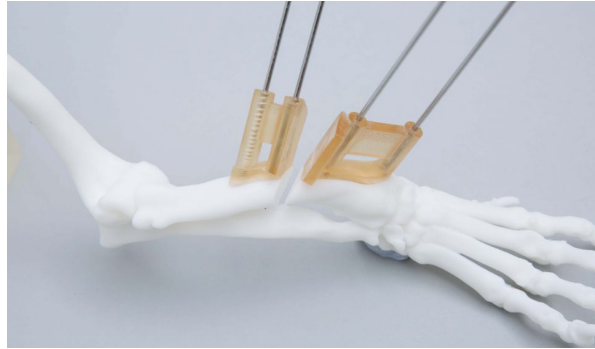


Figure 36: Reproduction of deformed bone together with the custom-made cutting and drilling guides to be used during the corrective orthopedic surgery. Image: courtesy of Bill Oxley.

While custom-made implants and surgical guides are the likely ideal solution, the main issue in the use of 3D technology on an individual basis is the cost in time and money, as well as the need for a surgical team to be familiar with 3D technologies (or the need to call on a third party intervention).

In humans, pathology-free individuals are selected to obtain 3D triangular-surface models of bones, extracted from computer tomographic data. These are used to encode characteristic shapes variations into statistical shape models (SSM) [Vlachopoulos et al, 2018]. SSM are used to predict the patient-specific anatomy in the injured or pathological patient, in order to achieve the most accurate surgery planning and bone reconstruction.

The use of SSM in veterinary medicine, could be beneficial in order to limit the absolute need to use patient-based technics. It would allow development of species-specific bone plates that could be of great value to surgeons (in terms of application ease), patient (in terms of recovery) and owner (financially more interesting). In the case where bones are found highly similar, SSM could be used for deformity corrections, fracture repair and surgical guide production... bringing a whole new era for orthopaedic surgery.

Patient-based tools and guides have been made possible thanks to the development of high-performance 3D printers. Nonetheless, the importance of manufacturing a universal-model orthopaedic plate comes from the remaining lack of precision that can be achieved by current 3D printers. The high precision delivered by traditional plate manufacturing - such as in the *Depuy Synthes* locking compression plate (LCP®) system, where screws are locked to the plate thanks to threaded screw heads, and corresponding threaded plate hole [AOFoundation, 2019] - is nowadays not possible to reproduce using 3D printers (yet!) [Oxley B. 2019].

4.15. Limitations: what mistakes might have been done and how to overcome them.

Lack of history from the cat population used in the study is the first limitation. The French population of cats, coming from a known veterinary practice, is assumed to be composed of a majority of mixed “European” breed, of unknown genetic background. The Hungarian

individuals, collected by the anatomy department of the university of Budapest, are from unknown origin. The latter were “split”, and only hindlimbs were kept while awaiting the bone cleaning process. It was therefore nearly impossible to identify their breeds, which may have given indication about size variations. Knowledge about the breed could have given the ability to separate populations into different groups with similar bone development. Differences observed in the French population compared to the Hungarian individuals supposes a separate, though slow, mutation of the cat species according to their geographical location. This theory cannot be verified due to the lack of information on breed, age and size: it could be due to a total coincidence. Furthermore, age, associated with the constant bone remodelling process [Demontiero O. et al, 2012] might be a plausible factor explaining differences found across individuals (such findings could lead to further studies: scan the skeleton of an individual across years to see its evolution). Weight, which could be considered as a factor of size (i.e. height), might have had a limited use if we consider overweight and obesity as more and more commonly observed disorders [German AJ. 2006]. Although, it would have been interesting to note whether weight has an impact on long term bone deformity (age + obesity = bone deformity?) such as a more pronounced valgus. Wither height, would have been plotted against the bone length, with an assumed linear relationship.

In our study, the length of the tibia is measured using a straight line traced between the area intercondylaris centralis and the cochlea. This technic, described in the litterature, does not take into account the bone curvatures and angulation of the cochlea [Figure 5]. Therefore, a margin of error is to be considered. The anatomical axis, travelling through the centre of the bone cortices, would be a more precise axis to use to measure the bone length [Figure 38]. It is interesting to note that, in the tracing of the anatomical axis described on 2D radiographs [Petazzoni M. et Jaeger GH., 2008], extremities of segments are kept identical to those used for the mechanical axis, although those landmarks are not necessarily positionned at the centre of the cortices. For the purpose of 3D measurements, it might be interesting to determine if those landmarks need to be redefined.

Accuracy of our measurements depends a lot on the CT scanning quality. In our case, the CT scanner hardware involves did not yield the best possible quality. This was mainly due to a scarcity of storing space and “memory available” when trying to launch the scanning process. While CT slices interval of 1mm can achieve a favourable quality on bigger specimens, the precision involved on bones measuring about 10cm in their length can be questioned. In the case of the medullary canal area evaluation, it is obvious that its measurement highly varies with CT and segmentation parameters, due to the remaining material in the shaft: we are rather measuring a reconstructed space than an anatomical structure.

Segmentation and 3D reconstruction is also highly dependent on the CT scanning quality, and, on top of the questionable scanning definition, it would appear that the scan interpretation of air-on-bone yields a different, less detailed / accurate, imaging result compared to flesh-on-

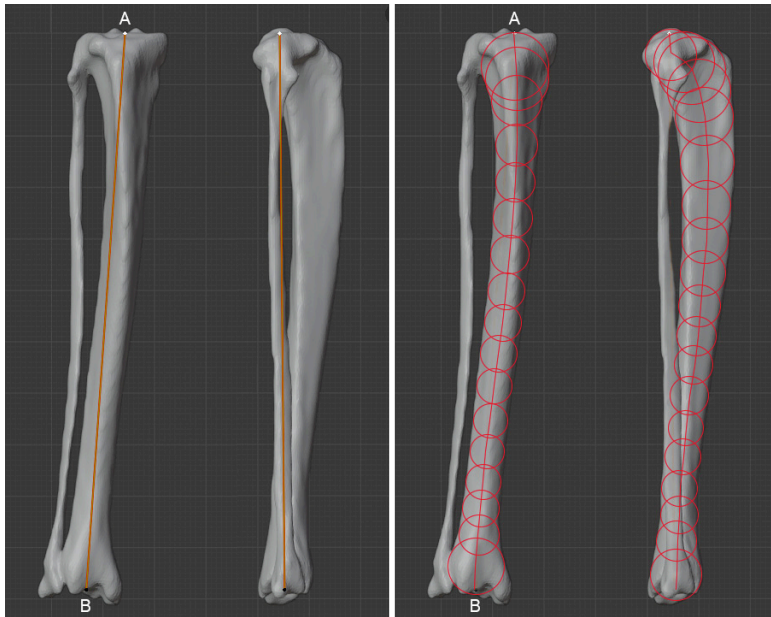


Figure 38: Orthographic view of the cat tibia in frontal and lateral view. Left: the length measured according to the mechanical axis: by a straight line traced between area intercondylaris centralis and the most proximal point of the cochlear ridge. Right: the length measured according the anatomical axis, line traced following the centre of circle traced along the bone cortices.

bone (and a way to counteract these artefacts is to dip the bones into jelly) [Oxley B., 2019]. Some bones, less mineralised, clearly do not have the same ability to absorb X-rays. Their reconstruction proved to be more difficult [Figure 37], and might have lead to less precise measurements.

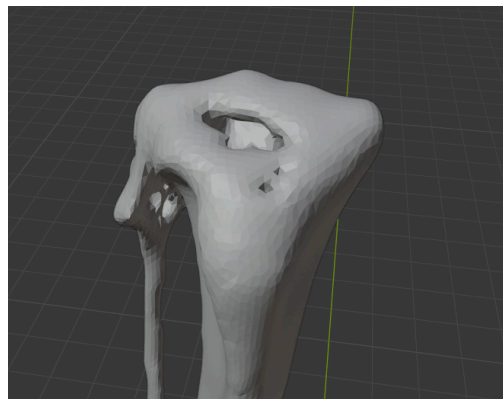


Figure 37: 3D reconstruction of cat tibia: zoom on proximal epiphysis presenting some artefacts, due to a poor CT definition.

After determining that cat tibiae are not “exactly similar”, however taking into account that some aspects of the bones have a tendency to remain in closed value ranges, we can wonder wether a population of thirty cats is too small of a sample to determine a possible tendency to follow a prevailing pattern. A bigger sample could comfort the theory that cats’ skeleton is highly different across individuals or could point towards a possible similarity pattern with the obvious few individuals who developed differences. That being said, having a bigger population to evaluate, coupled with manual work, would also bring a higher risk for errors. In such studies, automaticity would be a welcomed tool, and would also allow a much faster computing of information.

Lack of automaticity to perform measurements, and therefore the amount of manual work involved, increased the risk for “human error”. Additionally, 3D technology being fairly new in the medical field and not yet widespread, most measurement approaches are rather adapted to 2D imaging (X-ray). While the methods of angle measurements were re-adapted to the higher fidelity offered by 3D environment, the angle measurement tool only generates round numbers, and therefore lacks exactitude. Using solely the *CloudCompare*[®] software to compare bones to one another could have been the most automated technic, involving the least manipulation errors possible. Further studies with such process are to be considered.

When it comes to determining joints orientation/deviation, it was a disadvantage not to have kept both the femorotibial and tibiotarsal joints intact. The presence of the femur and tarsus would have greatly helped in determining the joints direction with more precision. Doing the study on disconnected bones made this detail difficult to achieve. The utility of four-dimensional CT as a novel method to investigate joint movement was recently demonstrated in dogs [Edamura K. et al, 2019]. 4D-CT involves making CT scans of the patient in multiple flexion-extension positions in order to create a 3D animation of the moving limb. 4D-CT can therefore evaluate the movement of the stifle joint both three-dimensionally and dynamically. This technic would demonstrate tibial torsion in the most precise manner, and would also prove to be useful for valgus measurements.

Tibial torsion measurements do not necessarily translate into the presence of a bony rotation along the bone: it does not give evidence of 3D torsion of the medial cortex along the tibial diaphysis. This should be an additional shape evaluation performed in the 3D environment. With regards to the proximal and malleolus angle, it would be interesting for both these angles to have a population distribution in order to know how far from the mean it could go for 95 and 99% of the population.

Our statistical analysis consisted mainly of mean values, standard deviations and coefficient of determination. For a real correlation analysis, it might be more interesting to use the Spearman’s rank correlation coefficient (r_s), which demonstrates how closely two sets of data are linked to each other.

4.16. Future studies

Since measurements and comparisons were undertaken on unilateral bones, it would now be appropriate to conduct another study to judge whether contralateral limbs are mirrored. Moreover, collecting bones with known breeds would add a valuable parameter. Doing scans on live animals (with history, follow-up, and various joint angles) would push the analysis beyond our results.

Measurement achieved have been adapted from 2D technics, originally developed to be used on radiographs. Therefore, the potential offered by the 3D environment and highly malleable

shapes was likely not used to its full potential. Technologies brought forward by CT scanning and 3D imaging can justify redefining the standard of measurements for various distances and angles. For instance, the method described to measure the TPA has proven to not be well adapted to the 3D shape of the tibial head. A future study could involve measuring TPA from lateral, medial and centre views, then evaluate a possible variability in angles, in order to create a novel evaluation technic.

The potential offered by *CloudCompare*[®], likely makes this software the most adapted tool to carry on further analysis and accomplish thorough shape comparison. However, past its capacity to determine how similar/different shapes are to each other, its sole use would not prove to be sufficient to compute statistical shape model (SSM), and construct a standard, mean, bone shape.

Upon wrapping up this study, several questions remain unanswered. Additional studies on this subject are to be considered in order to reach the original aim to develop universal, size-adapted orthopaedic plates, and several other, anatomically adapted surgical tools. To be produced, the design of an anatomical medial feline tibial plate (or interlocking nail), requires knowledge of the median length, cortical torsion & location, and proximal/distal angles. Since plates are applied medially, it is worth considering analysing solely the medial cortex of the bone. A cropped-shape comparison computed in *CloudCompare*[®] could lead to contrasted results. Furthermore, before producing such a plate, we need to determine / calculate its compatibility with the population.

5. CONCLUSION

Considering measurements carried out manually, we lean towards a heterogenous anatomy of the cat tibiae. They are in fact rather different from one individual to the next, although with some species-based similarities, especially when speaking about measured angles.

However, possible manipulation mistakes made during the process, coupled with the unexpected results obtained through the use of the 3D shape comparison algorithm, and Hausdorff distance principles, challenge this conclusion. It leads us to think that, with an automated process, we could obtain a very different outcome.

Subsequently, the combination of both approaches result in an inconclusive denouement. Further studies using automated evaluation are worthwhile. The creation of an accurate statistical shape model (SSM) of the tibia, would lead to ease in surgery planning and accurate bone reconstruction, and/or the elaboration of surgical implants and surgical tools.

6. SUMMARY

- **Objectives:** To investigate feline tibiae anatomy in order to determine how similar they are to one another, and evaluate the possibility to develop universal bone implants for i.e. fracture repair.
- **Material and methods:** CT scanning, coupled with 3D imaging are used on thirty-one cat tibiae. Measurements taken included tibial length, weight, proximal epiphysis circumference, smallest cortical circumference, smallest medullary area, angle between the malleolus and the cortex, angle between the proximal epiphysis and the cortex, valgus, tibial torsion and tibial plateau angle. 3D shape comparison between two sets of two bones was also undertaken.
- **Results:** Weight ($9.06\text{g}, \pm 1.73$) and proximal epiphysis circumference ($2.15\text{cm}, \pm 0.24$) were found to have a satisfactory relationship to the length variable ($107.15\text{mm}, \pm 4.83$). The smallest cortical circumference ($2.28\text{cm}, \pm 0.14$) and smallest medullary area ($10.5\text{mm}^2, \pm 3.1$) were found to have little statistical relationship to the length variable. The angle between the malleolus and the cortex ($157.13^\circ, \pm 4.16$), angle between the proximal epiphysis and the cortex ($163.7^\circ, \pm 4.01$), valgus ($16.51^\circ, \pm 4.41$), tibial torsion ($8.55^\circ, \pm 4.52$), and TPA ($30.32^\circ, \pm 2.62$), were found almost constant in all specimens and with no relationship to the bone length. The 3D shape comparison revealed a high similarity between bones evaluated, independently from being similar or different in length.
- **Conclusion and clinical significance:** Manually executed measurements did not orient the conclusion towards a similar anatomical shape across sizes. However, the computed 3D shape comparison experiment does not correlate to those results and brings yet unanswered questions that need to be explored in further studies. Given the latter results, the possibility to design an species-specific orthopaedic tibial plate is very much feasible.

References

- ‘3D reconstruction’ (2019) *Wikipedia*. URL: https://en.wikipedia.org/wiki/3D_reconstruction (Accessed: 30 October 2019)
- AOFoundation. (2019) *Locking versus nonlocking plates - Advantages to a locking plate/screw system*. URL: https://www2.aofoundation.org/wps/portal/!ut/p/a0/04_Sj9CPyKssy0xPLMnMz0vMAfGjzOKN_A0M3D2DDbz9_UMMDRyDXQ3dw9wMDAx8jfULsh0VAAdAsNSU!/?bone=CMF&contentUrl=%2Fsr%2Fpopup%2Fadditional_material%2F91%2FX40_Lockplate_principles.jsp&segment=Mandible&soloState=true#JumpLabelNr2 (Accessed: 10 November 2019)
- Aper R., Kowaleski MP., Apelt D., Drost WT. and Dyce J. (2005) *Computed tomographic determination of tibial torsion in the dog*. *Veterinary Radiology & Ultrasound*, Vol. 46, No. 3, pp 187–191.
- ‘Area’. (2011) *Math Open reference*. URL: <https://www.mathopenref.com/area.html> (Accessed: October 2019.)
- Arthrex (2014) *Clavicle Plates and Screws*. URL: <https://www.arthrex.com/shoulder/clavicle-plates-and-screws> (Accessed 1 November 2019)
- Barnes, D.M., Anderson, A.A., Frost, C., Barnes, J. (2015). *Repeatability and reproducibility of measurements of femoral and tibial alignment using computed tomography multiplanar reconstructions*. *Veterinary Surgery* 44, 85–93.
- Chakravorty D. (2019) *Standard Tessellation Language, STL File Format (3D Printing) – Simply Explained*. URL: <https://libguides.ioe.ac.uk/c.php?g=482485&p=3299860> (Accessed: 1 November 2019)
- *CloudCompare* version 2.11 [CAD software] Available at: <http://www.cloudcompare.org/> (downloaded: 1 November 2019)
- ‘Coefficient of determination’ (2019) *Wikipedia*. URL: https://en.wikipedia.org/wiki/Coefficient_of_determination (Accessed: 2 november 2019)
- Creadditive (2019) *Creadditive Markets First 3D-Printed Veterinary Surgical Implant*. URL: <http://www.creadditive.ca/en/1710/> (Accessed: Sept 2019)
- D’Amico, L.L., Xie, L., Abell, L.K., Brown, K.T. and Lopez, M.J. (2011). *Relationships of hip joint volume ratios with degrees of joint laxity and degenerative disease from youth to maturity in a canine population predisposed to hip joint osteoarthritis*. *American Journal of Veterinary Research* 72, 376–383.
- Demontiero O., Vidal C. and Duque G. (2012) ‘Aging and bone loss: new insights for the clinician.’ *Therapeutic Advances in Musculoskeletal Diseases*. 2012 Apr; 4(2): 61–76. URL: <https://www.ncbi.nlm.nih.gov/pmc/articles/PMC3383520/>
- *DICOM Library* (2019). URL: <https://www.dicomlibrary.com/dicom/> (Accessed: 1 November 2019)
- Dunlap AE., Matthewa KG., Walters BL., Bruner KA., Ru H. and Marcellin-Little DJ. (2018) *Three-dimensional assessment of the influence of juvenile pubic symphysiodesis on the pelvic geometry of dogs* *AJVR*, Vol 79, No. 11.
- Evans HE. and De Lahunta A. (2013) *Miller’s Anatomy of the Dog*. 4th edn. Missouri. Saunders. pp. 148-151.
- Edamura K, Ichimura H, Tanegashima K, Yamazaki A, Tomo Y, Seki M, Asano K. and Hayashi K. (2019) ‘Analysis of joint movement in canine stifle joint using 4DCT’, *ECVS 2019: Small animals proceedings*, Budapest, 6 July 2019. p.159
- Fedorov A., Beichel R., Kalpathy-Cramer J., Finet J., Fillion-Robin J-C., Pujol S., Bauer C., Jennings D., Fennessy F., Sonka M., Buatti J., Aylward S.R., Miller J.V., Pieper S. and Kikinis R. (2012) ‘3D Slicer as an Image Computing Platform for the Quantitative Imaging Network. *Magnetic Resonance Imaging*.’ Nov;30(9):1323-41. PMID: 22770690. [Software] 3DSlicer version 4.10.2. <https://slicer.org>

- German AJ. (2006) 'The growing problem of obesity in dogs and cats.' J Nutr. 2006 Jul; 136(7 Suppl): 1940S-1946S.
- Hamilton-Bennett SE., Oxley B. and Behr S. (2017) 'Accuracy of a patient-specific 3D printed drill guide for placement of cervical transpedicular screws.' ECVN-ESVN 29th annual symposium in Edinburgh. DOI: <https://doi.org/10.1111/vsu.12734>
- Hudson L. and Hamilton W. (2010) *Atlas of Feline Anatomy for Veterinarians*. 2nd edn. Jackson, Teton media. p.35.
- 'Image segmentation' (2019) *Wikipedia*. URL: https://en.wikipedia.org/wiki/Image_segmentation (Accessed: 22 October 2019.)
- König HE. (2004) *Veterinary Anatomy of domestic animal, textbook and colour atlas*. 2nd edn. Edited by Liebich HG.
- Langley-Hobbs SJ. (2019) 'Feline Stifle Update - Cranial Cruciate Ligament Disease', *ECVS 2019: Small animals proceedings*, Budapest, 5 July 2019. p.51
- Longoa F., Nicetto T., Banzato T., Savioc G., Drigo M., Meneghelli R., Concheric G. and Isolaa M. (2017) 'Automated computation of femoral angles in dogs from three-dimensional computed tomography reconstructions: Comparison with manual techniques.' *The Veterinary Journal* 232 (2018) 6–12. URL: <https://doi.org/10.1016/j.tvjl.2017.11.014>
- Marcellin-Little DJ. (2019) *3D Printing and what it brings to the table*. [Webinar]. URL: <http://aofoundation-na.adobeconnect.com/p91ljfjylm1e/> (Accessed: 31 October 2019)
- Mindner JK, Bielecki MJ, Scharvogel S. and Meiler D. (2016) *Tibial plateau levelling osteotomy in eleven cats with cranial cruciate ligament rupture*. *Vet Comp Orthop Traumatol.* 23;29(6):528-535
- 'Orthographic projection' (2019) *Wikipedia*. URL: https://en.wikipedia.org/wiki/Orthographic_projection (Accessed: 2 November 2019)
- Oxley B, (2019). Conversation with Alexandre Caron, 25 October. [Personal Communication]
- Petazzoni M. and Jaeger GH. (2008) *Atlas of clinical goniometry and radiographic measurements of the canine pelvic limb*. 2nd edn. Meril Italia. p. 60-71.
- Schaller O., Constantinescu GM., Habel RE., Sack WO., Simoens P. and De Vos N. (2007) *Illustrated veterinary anatomical nomenclature*. 2nd edn. Enke Verlag in. pp.68-71.
- Schmierer PA. (2019) 'MIPO-Is there any difference in cats compared to dogs,' *ECVS 2019: Small animals proceedings*, Budapest, July 2019. p.58
- Singhal N. (2004) 'Shape matching and structural comparison', *CS273: Algorithms for Structure and Motion in Biology*. Stanford University. Unpublished.
- Smith EJ., Marcellin-Little DJ., Harryson OL. and Griffith EH. (2017) *Three-dimensional assessment of curvature, torsion, and canal flare index of the humerus of skeletally mature nonchondrodystrophic dogs*. *AJVR*, Vol 78, No. 10.
- Svirin A. (2019) 'Three-Dimensional Coordinate System.' URL: <https://www.math24.net/three-dimensional-coordinate-system/> (Accessed: October 2019.)
- The Blender Foundation. (2019) *Blender* version 2.80 [CAD software]. Available at: <https://www.blender.org/download/> (downloaded: 18 September 2019)
- The horos project. (2018) Horos™ version 3.5.5. [medical imaging software] Available at: <https://horosproject.org> (downloaded: 29 June 2019)
- Vlachopoulos L., Luthi M., Carrillo F., Gerber C., Szekely G. and Furnstahl P. (2018.) *Restoration of the patient-specific anatomy of the proximal and distal parts of the humerus: statistical shape modeling versus contralateral registration method*. *Journal Bone Joint Surgery America*. 100(8):e50. DOI: <https://doi.org/10.2106/JBJS.17.00829>

Annexes

Annexe 1: detailed measurements made on each cat tibia.

Ref	known details	weight (g)	weight of L	Top coordinates			Bottom coordinates			length (mm)	length in Blender
				X	Y	Z	X	Y	Z		
F1	Eu, F, 2.5kg, 15yo	9.13	9.3	157.146	21.6	216	153.422	21.036	109	107.07	108.40
F2		9.08	9.28	-101.935	5.426	116	-95.394	5.741	6	110.19	
F3		14.72	14.83	18.827	18.504	226	20.759	16.593	109	117.03	115.92
F4	Eu, M, 4kg, 11yo	9.82	9.37	20.198	3.763	121	24.473	5.1	9	112.09	
F5		14.43	14.68	70.366	18.525	226	68.613	18.199	111	115.01	
F6	Eu, F, 4kg, 15yo	8.68	8.61	20.702	4.361	-10	23.807	3.051	-112	102.06	
F7	Eu, M, 3yo	11.99	11.93	81.55	4.96	121.00	81.62	4.30	12.00	109.00	112.17
F8		10.92	10.92	79.11	6.34	-4	82.009	3.589	-116	112.07	
F9		9.69	9.51	-38.797	5.248	-11	-34.679	3.659	-117	106.09	
F10	Main coon	13.75	13.28	-98.346	6.434	-17	-94.935	4.846	-147	130.05	
F11		11.43	11.73	75.769	4.573	251	78.93	2.849	139	112.06	
F12	Main coon	14.03 /									122.67
F13		7.1	7.3	-87.894	-31.618	-168	-89.423	-28.821	-267	99.05	98.47
F14		8.24	8.52	9.54	1.874	246	14.094	2.559	138	108.10	
F15		6.98	7.04	-48.237	2.876	238	-46.675	1.343	138	100.02	101.80
H1		13	12.93	205.066	18.584	98	201.946	18.824	-18	116.04	
H2		8.92	8.3	23.065	14.359	-26	20.685	18.087	-140	114.09	
H3		8.7	8.8	75.567	15.89	-31	69.966	19.278	-143	112.19	
H5		7.7	7.64	117.602	16.748	96	112.247	18.326	-10	106.15	
H6		8.17	8.09	68.69	14.969	98	69.15	18.325	-7	105.05	
H7		7.27	7.3	22.874	3.898	-123	20.83	2.624	-224	101.03	102.15
H8		9.13	9.04	207.821	21.874	213	204.103	21.264	107	106.07	
H9		8.04	8.1	19.141	13.839	97	17.728	16.533	-8	105.04	
H11		7.68	8.88	121.684	21.221	217	118.485	20.641	111	106.05	
H13		8.67	8.86	178.546	16.38	-33	172.941	19.471	-146	113.18	113.60
H14		9.56	9.38	127.572	17.696	-30	119.275	19.76	-139	109.33	
H15		7.55	7.65	122.198	18.443	-156	117.913	19.362	-260	104.09	
H16		6.7	6.57	73.415	18.205	-162	71.181	19.979	-259	97.04	96.95
H17		9.95	9.8	172.976	17.06	-163	166.926	19.805	-266	103.21	
H18		10.1 /		158.851	18.939	95	148.103	19.179	-15	110.52	

Ref	smallest circ. area (mm2)	smallest circ contour (cm)	@ Z coord	distance from bottom	ratio %	min medulla area	distance from bottom	ratio %	distance from bottom	ratio %	Prox. epiph. area (cm2)
F1	36.703	2.155	138	-29	0.3718	10.298	40	0.596	40	0.596	1.908
F2	44.198	2.373	31	25	0.2941	10.793	42	0.616	42	0.616	2.201
F3	54.807	2.656	136	27	0.3000	9.722	160	1.294	160	1.294	2.533
F4	42.005	2.33	24	15	0.1546	8.863	46	0.696	46	0.696	2.119
F5	53.843	2.639	132	21	0.2234	11.239	45	0.643	45	0.643	2.661
F6	38.66	2.241	-90	22	0.2750						1.841
F7	45.547	2.428	38	26	0.3133						2.337
F8	47.351	2.481	-82	34	0.4359	11.179	46	0.696	46	0.696	2.394
F9	39.769	2.259	-89	28	0.3590	8.982	43	0.682	43	0.682	1.986
F10	49.495	2.539	-117	30	0.3000						2.928
F11	48.571	2.505	172	33	0.4177	10.298	48	0.749	48	0.749	2.518
F12	57.665	2.701	-219	19	0.2375	1.143	47	0.903	47	0.903	2.887
F13	36.764	2.173	-248	34	0.4595	9.556	47	0.769	47	0.769	1.964
F14	32.464	2.067	172	27	0.3699	4.729	47	0.886	47	0.886	2.271
F15	35.321	2.142	165	23	0.2473	14.184	32	1.320	32	1.320	1.787
H1	48.084	2.531	5	16	0.1633	14.776	-100	0.541	-100	0.541	2.131
H2	42.094	2.322	-124	26	0.3023	13.903	-99	0.647	-99	0.647	2.172
H3	40.994	2.295	-117	15	0.1648	9.658	32	0.656	32	0.656	2.277
H5	36.028	2.166	5	25	0.3125	11.272	33	0.615	33	0.615	2.092
H6	40.195	2.272	18	40	0.6557						1.885
H7	36.838	2.181	-184	24	0.2927	5.871	152	0.738	152	0.738	2.002
H8	36.164	2.161	131	18	0.2069	10.798	35	0.694	35	0.694	
H9	36.69	2.169	10	25	0.3086	11.315	157	0.767	157	0.767	
H11	46.052	2.433	136	29	0.3452	8.121	-125	0.228	-125	0.228	2.415
H13	41.673	2.309	-117	30	0.3797	15.026	-96	0.652	-96	0.652	2.153
H14	46.433	2.424	-109	10	0.1064	9.531	-211	0.891	-211	0.891	1.845
H15	38.776	2.24	-250	21	0.2763	5.682	-218	0.732	-218	0.732	1.768
H16	32.753	2.058	-238	29	0.3919						2.226
H17	44.817	2.39	-237	18	0.1957	7.674	24	0.515	24	0.515	
H18	38.64	2.243	3	18	0.1957						

HuVetA
ELECTRONIC LICENSE AGREEMENT AND COPYRIGHT DECLARATION*

Name: Cécile JESTIN

Contact information (e-mail): cecile.jestin@gmail.com

Title of document: Three-Dimensional Morphological Comparison of Feline Tibiae

Publication data of document: 22nd November 2019.

Number of files submitted: One

By accepting the present agreement, the author or copyright owner grants non-exclusive license to HuVetA over the above mentioned document (including its abstract) to be converted to copy protected PDF format without changing its content, in order to archive, reproduce, and make accessible under the conditions specified below.

The author agrees that HuVetA may store more than one copy (accessible only to HuVetA administrators) of the licensed document exclusively for purposes of secure storage and backup, if necessary. You state that the submission is your original work, and that you have the right to grant the rights contained in this license. You also state that your submission does not, to the best of your knowledge, infringe upon anyone's copyright. If the document has parts which you are not the copyright owner of, you have to indicate that you have obtained unrestricted permission from the copyright owner to grant the rights required by this Agreement, and that any such third-party owned material is clearly identified and acknowledged within the text of the licensed document.

The copyright owner defines the scope of access to the document stored in HuVetA as follows: *I grant unlimited online access.*

In-house accessibility of the document: *I grant in-house access (namely, reading the hard copy version of the document) at the Library.*

If the preparation of the document to be uploaded was supported or sponsored by a firm or an organization, you also declare that you are entitled to sign the present Agreement concerning the document.

The operators of HuVetA do not assume any legal liability or responsibility towards the author/copyright holder/organizations in case somebody uses the material legally uploaded to HuVetA in a way that is unlawful.

Nantes, 22nd November 2019

Author/copyright owner signature

